



Climate & Ecology in the Rocky Mountain Interior After the Early Eocene Climatic Optimum

Rebekah A. Stein^{1,2}, Nathan D. Sheldon¹, Sarah E. Allen³, Michael E. Smith⁴, Rebecca M. Dzombak¹, Brian R. Jicha⁵

5 ¹Department of Earth & Environmental Sciences, University of Michigan, Ann Arbor, MI, 48109, USA

²Department of Earth & Planetary Sciences, University of California, Berkeley, CA, 94720, USA

³Department of Biology, Penn State Altoona, Altoona, PA, 16601

⁴School of Earth & Sustainability, Northern Arizona University, Flagstaff, AZ, 86011, USA

⁵Department of Geosciences, University of Wisconsin-Madison, Madison, WI 53706

10 *Correspondence to:* Rebekah A. Stein (restein@berkeley.edu), Nathan D. Sheldon (nsheldon@umich.edu)

Abstract. As increasing atmospheric carbon dioxide (CO₂) and temperatures accompany modern climate change, ancient hothouse periods become a focal point for understanding ecosystem function under similar conditions. The early Eocene exhibited high temperatures, high CO₂ levels, and similar tectonic plate configuration to today, so it has been invoked as an analog to modern climate change. During the early Eocene, the greater Green River Basin (GGRB) of southwest Wyoming
15 was covered by an ancient hypersaline lake (Lake Gosiute; Green River Formation) and associated fluvial and floodplain systems (Wasatch and Bridger Formations). The volcanoclastic Bridger Formation was deposited by an inland delta that drained from the northwest into freshwater Lake Gosiute and is known for its vast paleontological assemblages. The Blue Rim escarpment exposes approximately 100 meters of the lower Bridger Formation, which includes plant and mammal fossils, paleosols and organic remains suitable for geochemical analyses, as well as ash beds and volcanoclastic sandstone beds suitable
20 for radioisotopic dating. New ⁴⁰Ar/³⁹Ar ages from the middle and top of the Blue Rim escarpment constrain age of its strata to ~49.5–48.5 Ma ago, during the “falling limb” of the early Eocene climatic optimum. Using several geochemical tools, we reconstructed provenance and parent material in both the paleosols and the associated sediments and found no change in sediment input source despite significant variation in sedimentary facies and organic carbon burial. We also reconstructed environmental conditions at the time, including temperature and precipitation (from paleosols) and the isotopic composition
25 of CO₂ from plants found in the floral assemblages, before comparing them to reconstructions for the same time made using leaf physiognomic techniques and marine proxies. The paleosol-based reconstructions (near the base of the section) of precipitation (608–1167 mm yr⁻¹) and temperature (10.4 to 12.0 °C) were within error of, although lower than, those based on



floral assemblages, which were stratigraphically higher in the section. Geochemistry and detrital feldspar geochronology indicate a consistent provenance for Blue Rim sediments, sourcing predominantly from the Idaho paleoriver, which drained the active Challis volcanic field. Thus, because there was neither significant climatic change nor significant provenance change, variation in sedimentary facies and organic carbon burial likely reflected localized geomorphic controls, and the relative height of the water table. The ecosystem can be characterized as a wet, subtropical forest throughout the interval based upon the floral humidity province and Holdridge life zone schemes. Given the mid-paleolatitude position of the Blue Rim Escarpment, those results are consistent with marine proxies that indicate that globally warm climatic conditions continued beyond the peak warm conditions of the early Eocene climatic optimum. The reconstructed atmospheric $\delta^{13}\text{C}$ value (-5.3 to -5.8‰) closely matches both the independently reconstructed value from marine microfossils (-5.4‰), as well as the isotopic composition of the mantle (-5.4‰), suggesting that the warm conditions were maintained by volcanic outgassing.

1 Introduction

1.1 The Eocene Period as an Analogue for a Future Warm World

The anthropogenic release of fossil fuels drives a rapid and sustained increase in atmospheric carbon dioxide (CO_2) that is coupled with climate change (IPCC 2007). To understand the effects of elevated CO_2 on the Earth (e.g., Cotton et al., 2013), we seek out geological periods with high temperatures and high atmospheric CO_2 for comparison. The early Eocene climatic optimum (EECO) has been invoked as a climate analog for our projected future (e.g., Zhu et al., 2019). This warming during the EECO occurred 53–50 million years ago, with peak warming from 51.5–50.9 Ma; this period consisted of long-term global temperature maxima and high CO_2 levels but was tectonically comparable to today (Hyland & Sheldon 2013; West et al., 2020). From the Paleocene to early Eocene, it has been inferred that much of North America was warm and wet, with extensive temperate forests (Smith et al., 2012; Breedlovestrout et al., 2013; Greenwood et al., 2016; West et al., 2020) up to high latitudes 65 °N (Dillhoff et al., 2013). As the planet warms, there is increasing concern about water availability and dry climates getting drier. For example, the North American Southwest, a high-elevation desert, is at risk for having its already severe droughts increased in frequency and severity (Poore et al., 2005; Cheeseman 2016). Therefore, the study of ancient climate and ecosystems informs understanding of these emerging climate and societal challenges.



1.2 Continental interior and foreland basins in the Rocky Mountains

55 The marine foreland of the North American Cordillera was partitioned into a series of terrestrial basins by an anastomosing network of Laramide basement structures during the Paleogene, likely due to coupling between the shallow Farallon slab with the North American lithosphere (Dickinson et al., 1988; Snoke et al., 1993; DeCelles, 2004). These basins accumulated several kilometers of lacustrine and fluvial strata during the Paleocene and early Eocene and led to formation of a series of large lakes (Smith et al., 2008). High sediment accumulation rates in these basins contributed locally to excellent
60 preservation of the biota, allowing us to study deep time at high resolution (Looy et al., 2014). The carbonate-rich lacustrine Green River Formation was deposited from Lake Gosiute within the greater Green River Basin (Fig. 1). The predominantly siliciclastic Wasatch and Bridger formations reflect contemporaneous fluvial and floodplain deposition adjacent to Lake Gosiute.

The greater Green River Basin lies to the east of the Sevier fold and thrust belt, and is bounded on the north, east and
65 south by Laramide basement structures, each of which likely contributed water and sediment to the basin (Smith et al., 2008; Smith et al., 2014). The basin also likely received water and sediment at times from paleoriver(s) which drained the high-elevation Cordilleran hinterland to the west (Chetel & Carroll, 2010; Chetel et al., 2011; Smith et al., 2014). Over two kilometers of terrestrial strata accumulated in its depocenter during the Paleogene. The paleolatitude of southwest Wyoming in the early Eocene (41–41.82 °N; Wolfe et al., 1998; Hyland & Sheldon 2013) is thought to be relatively comparable to its
70 position today, thus changes in the climate of this region are not related to changes in latitude, and instead are related to global and regional climate.

1.3 Using multiple proxies to characterize an environment

There are several terrestrial proxies that can be used to reconstruct paleoclimate and paleoecology (e.g., pedogenic carbonate isotope values, floral assemblages, stomatal density; Cerling 1992; Royer 1999; Wilf 2000; Spicer et al., 2009). The
75 preservation of abundant, high-quality organic and inorganic specimens and samples due to the tectonic assemblage of the basin, makes the GGRB an excellent location for a multi-proxy approach. Organic geochemistry can be used to demonstrate isotopic composition of the atmosphere, which reflects sources of CO₂ gas to the atmosphere ($\delta^{13}\text{C}_{\text{atm}}$; Keeling 1979; Boutton



1991; Deines 1992; Arens et al., 2000; Stein et al., 2019). Multiple inorganic geochemistry proxies (see methods) can provide context for the depositional environment, climate, hydroclimate, age, and origin of sediments. This study seeks to combine
80 these proxies to create a holistic reconstruction of the greater Green River Basin (GGRB) during the early Eocene using the extensive deposits of the Blue Rim escarpment.

2 Description of locality

The Bridger Formation is an approximately 842 m thick series of tuffaceous deltaic-alluvial and minor lacustrine
85 sedimentary strata which overlie and interfinger with the Green River Formation (Koenig 1960; Kistner 1973; Murphey & Evanoff 2001; Clyde et al., 2001). Vertebrate fossils collected from the Bridger Formation formed the basis for defining the Bridgerian North American Land Mammal ‘age’ (“NALMA”; e.g., Osborn 1909; Wood et al., 1941; Van Houten 1944; Gingerich et al., 2003; Robinson et al., 2004). Mapping and biostratigraphy have permitted further subdivision of the Bridger Formation into intervals A-E (Matthew 1909; Murphey & Evanoff 2001; Murphey et al., 2011). Several volcanic ash horizons
90 within the Bridger Formation and the underlying Green River Formation have been radioisotopically dated using $^{40}\text{Ar}/^{39}\text{Ar}$ geochronology to have accumulated between approximately 50 Ma and 46 Ma (Fig. 1; Table S2; Murphey & Evanoff 2001; Smith et al., 2008). Strata exposed along the Blue Rim study area represent the oldest exposed portion of the Bridger Formation. Unlike much of the Bridger Formation, these ‘Bridger A’ deposits have not been radioisotopically dated, but regional mapping and correlations suggests they were deposited above the Sand Butte bed of the Laney Member of the Green River Formation,
95 and likely occur beneath the more extensively mapped Bridger B interval (Murphey & Evanoff 2001), bracketing a depositional age between the ca. 50 Ma ‘6th tuff’ of the Green River Formation and the ca. 49 Ma age for the Church Butte tuff, which occurs within Bridger B (Fig. 1).

Several potential sediment sources may have contributed to the Bridger Formation: including siliciclastic material derived from surrounding uplifts; volcanoclastic and siliciclastic sediment delivered by the Idaho paleoriver (Chetel et al.,
100 2011); volcanic ashfall from the Challis and Absaroka volcanic fields; and autochthonous lacustrine carbonates (Murphey & Evanoff 2001; Fig 1a). Whereas the older, and in part coeval Laney Member of Green River Formation is composed primarily of carbonate lacustrine sediments, the Bridger Formation is composed principally of siliciclastic sediment, with several minor



intervals of lacustrine carbonate (Buchheim et al., 2000; Murphey & Evanoff 2001). Sediment accumulation during Bridger Formation deposition appears to have been relatively continuous in the basin center based on existing age control (Murphey & Evanoff 2001). Because of this, the Bridger Formation has pristine faunal and floral preservation, making it an excellent candidate for understanding ecosystem function (Brand et al., 2000; Allen et al., 2015; Allen 2017b).

The Bridger Formation is exposed laterally over 12 kilometers at Blue Rim and is locally approximately 100 m thick (Kistner 1973). The flora at Blue Rim has been collected and described in great depth and is known for the preservation of all plant organs and tissues including leaves, flowers, fruits, seeds, wood, pollen, and spores (Allen 2017a/b). Eocene floral assemblages at Blue Rim occupy warm, subtropical, wet biomes; angiosperms including palms were abundant and dicotyledonous taxa were up to 28 m tall (Allen 2015; Allen 2017a/b), antithetical to the dry scrub desert found at Blue Rim escarpment today. Of the multiple quarries, the lower horizon (older) floral assemblage consists of taxa such as the abundant climbing fern *Lygodium kaulfussii* (fern, Lygodiaceae), “dicots” like “*Serjania*” *rara* (soapberry, Sapindaceae), *Populus cinnamomoides* (poplar, Salicaceae) and *Landeenia arailiodes* (Sapindales, *Goweria bluerimensis* (Icacaceae), and *Phoenix windmillis* (palm; Arecaceae; Allen 2015; Allen et al., 2015; Allen 2017b). The upper horizon preserves taxa such as *Macginitiea wyomingensis* (sycamore; Platanaceae), *Populus cinnamomoides* (poplar, Salicaceae), *Cedrelospermum nervosum* (elm; Ulmaceae), “*Serjania*” *rara* (soapberry, Sapindaceae), and many more (Allen 2017b).

3 Methods

120 3.1 Geochronology

Volcaniclastic beds were sampled from the Blue Rim escarpment for $^{40}\text{Ar}/^{39}\text{Ar}$ geochronological dating: two samples from the prominent ‘blue-green marker’ unit that occurs approximately halfway up the section; and two sand beds that crop out near the top of the exposure. To prepare sanidine phenocrysts for analysis, samples were crushed, leached in dilute hydrochloric acid (HCl) and hydrofluoric acid (HF) prior to hand-picking of sanidine in refractive index oils using a petrographic microscope, and then ultrasonic cleaning in acetone and ethanol. Sanidine phenocrysts from sampled ash beds were irradiated adjacent to standard sanidine crystals from Fish Canyon tuff (FCs) in cadmium shielding within the TRIGA (Training, Research, Isotopes, General Atomics) water-cooled, low-enriched uranium/zirconium fuel reactor at Oregon State



University. Single sanidine crystals were fused using a 25W CO₂ laser and then analyzed for ⁴⁰Ar/³⁹Ar composition using a
MAP 215-50 mass spectrometer attached to a metal ultra-high vacuum (UHV) gas extraction and clean-up line at the University
130 of Wisconsin Madison WiscAr laboratory. A 28.201 Ma age for Fish Canyon sanidine standard (FCs; Kuiper et al., 2008) was
used to calculate apparent ages for each laser fusion analysis, and weighted mean ages were calculated for the youngest
coherent population of sanidine dates from each sample. For populations that exceed an MSWD of 1, uncertainties in the
weighted mean were multiplied by the inverse of the square root of the MSWD to reflect the additional uncertainty implied by
the associated age scatter.

135

3.2 Physical Measurements

3.2.1 Stratigraphy and fossils

Starting at the base of the Blue Rim escarpment, adjacent to the first sampled paleosol (Fig. 2), an updated
stratigraphic column was measured (41.7985 °N, -109.5856 °E) in September 2019 (Fig. 3, 4, 5, 6, 7). This 67 m stratigraphic
140 column traced the flanks of the escarpment to the top of the badlands. The stratigraphic column was sampled every 3 m
(approximately the height of two Jacob-staffs) or at every interval of visual change (color, texture). In addition, plant fossils
and plant hash were quarried at two locations approximately halfway (26 m, 33 m) and close to the top of the stratigraphic
section (51.5 m, 52 m) for organic-rich fossil samples for isotope and bulk chemistry analysis.

145 3.2.2 Paleosol sampling

Six profiles of the same paleosol were identified and excavated along a lateral transect at the base of the Blue Rim
escarpment (41.79892625, -109.58362614, WGS 1984 (19BRWY1); Fig. 7, S8). Paleosols sampled by horizon based on
pedogenic features including root traces, burrows, drab-haloes and kerogenized roots, and horizonation (Fig. S1a, Table S1).
Fresh rock material was excavated by digging at least 20 cm into the surface, avoiding all traces of modern pedogenesis or
150 surficial climate influence (i.e., modern roots or carbonate nodules). One distinctive, laterally continuous paleosol at the base
of the section was sampled in five individual profiles over 440 m (Fig. 3; Fig. S1, S2, 19BRWY2-6). Samples were collected
from each horizon present, with no fewer than three samples per paleosol profile. At each location, every present horizon (O,



A, B, C) was sampled. For horizons that had color, texture, and/or other physical intra-horizonal changes, multiple samples were collected.

155

3.2.3 Isotope analyses

Paleosol samples were ground to 70 μm in a shatterbox. Approximately 10 g aliquots of samples were weighed out and then acidified in 5% hydrochloric acid (HCl) for 30 minutes to remove carbonate and leave behind total organic carbon of bulk sample. After 30 minutes, these samples were decanted, then re-acidified for a total of three times (and/or until solution stopped bubbling). After these acid washes, they were rinsed with deionized water three times (or more, if given >3 acid washes). Samples were then dried in an oven at 50 $^{\circ}\text{C}$ for 72 hours.

Between 20–25 mg of each sample was loaded into tin capsules and run on a Costech Elemental Analyzer to determine weight %C and %N in University of Michigan's Earth Systems Lab with acetanilide (71.09 %C, 10.36 %N) for elemental composition calibration and acetanilide and atropine (70.56 %C, 4.18 %N) standards. The %C was used to calculate idealized loading size for isotope analysis; these samples were then run on the Picarro Cavity Ring-Down Spectroscopy (CRDS) on low carbon (Mode 9) for organic carbon isotope values ($\delta^{13}\text{C}_{\text{org}}$), with external precision better than $\pm 0.3\%$ for low-carbon samples.

165

3.2.4 Bulk geochemistry

Approximately 10 g aliquots of crushed paleosols, mudstone, and siltstone were measured and sent to ALS Laboratories in Vancouver, British Columbia, Canada for bulk elemental analysis. At ALS, samples were digested with perchloric (HClO_4), hydrofluoric (HF), nitric (HNO_3) and hydrochloric (HCl) acids, and concentrations were determined by inductively coupled plasma (ICP) optical emission spectrometry and ICP-mass spectrometry. The ICP-OES and ICP-MS were calibrated using internal standards, with major element precision better than 0.2 weight %.

170

175 3.3 Paleoclimatic and Paleoenvironmental Calculations

3.3.1 Weathering indices and leaching



Weathering was quantified using Chemical Index of Alteration of B horizons (CIA; Equation 1; Nesbitt & Young 1982), a feldspar weathering index based on the discrepancy in ion mobility during weathering.

$$CIA = \frac{Al_2O_3}{Al_2O_3 + Na_2O + CaO + K_2O} \times 100 \quad (1)$$

180

To test for alteration and expected pedogenic elemental trends, changes in individual element mobility and strain were explored using mass balance (Equations 2–3; Chadwick et al., 1990), where ε represents the strain on an immobile element like Ti or Zr and τ represents the relative gain or loss of a mobile element relative to the paleosol's parent material. Average values of 2.7 g cm^{-3} and 1.5 g cm^{-3} were used for reworked ash and soil density, respectively (e.g., Sheldon & Tabor, 2009).

185

$$\tau_{j,w} = \frac{(\rho_w C_{j,w})}{(\rho_p C_{j,p})} \times [\varepsilon_{i,w} + 1] - 1 \quad (2)$$

$$\varepsilon_{i,w} = \frac{(\rho_p C_{j,p})}{(\rho_w C_{j,w})} - 1 \quad (3)$$

The Paleosol Weathering Index (PWI; Equation 4; Gallagher & Sheldon 2013), which is based on differential bond strengths in cation oxides, provided additional means for examining weathering. Molar concentrations are used to make calculations in Equations 1–4, rather than elemental concentrations.

190

$$PWI = ((4.20 * Na) + (1.66 * Mg) + (5.54 * K) + (2.05 * Ca)) * 100 \quad (4)$$

We used several geochemical proxies to examine intensity of leaching, including the ratio of barium to strontium (Ba/Sr), which is higher with more leaching and lower with less leaching (Sheldon 2006; Retallack 2001) due to differential solubility; Sr is more soluble than Ba (Vinogradov 1959). The ratio of the sum of base cations to titanium is another metric for leaching, under the assumption that titanium is immobile, while other bases are mobile (Sheldon & Tabor 2009). The ratio of the sum of base cations to aluminum has been used as a metric for hydrolysis (Retallack 1999; Bestland 2000; Sayyed & Hundekari 2006).

195

200 3.3.2 Provenance and Parent Material



The molar ratios of titanium to aluminum (Ti/Al) and zirconium to aluminum (Zr/Al) was used to screen for consistency in sediment source in soils; direction of change in Ti/Al ratios is related to differences in chemical weathering, while Zr/Al ratios are related to changes in physical weathering (Sheldon & Tabor 2009). The molar ratio of uranium to thorium (U/Th), and lanthanum to cerium (La/Ce) were used to trace potential changes in parent material composition through the stratigraphic unit, where a constant down-profile U/Th and La/Ce ratios reflect single-parent source (Sheldon 2006; Sheldon & Tabor 2009). Absolute parent material values for each of these ratios are not well calibrated, but direction of change observed at any site indicates a change in parent material, U/Th is redox-sensitive, so La/Ce ratios are used as a comparative point in case of highly reduced environments.

The molar ratios of titanium to aluminum (Ti/Al) and zirconium to aluminum (Zr/Al) was used to screen for consistency in sediment source in soils; direction of change in Ti/Al ratios is related to differences in chemical weathering, while Zr/Al ratios is related to changes in physical weathering (Sheldon & Tabor 2009). The molar ratio of uranium to thorium (U/Th), and lanthanum to cerium (La/Ce) were used to trace potential changes in parent material composition through the stratigraphic unit, where a constant down-profile U/Th and La/Ce ratios reflect single-parent source (Sheldon 2006; Sheldon & Tabor 2009). Absolute parent material values for each of these ratios are not well-calibrated, but direction of change observed at any site indicates a change in parent material, U/Th is redox-sensitive, so La/Ce ratios are used as a comparative point in case of highly reduced environments.

3.3.3 Paleoclimate reconstructions using foliar assemblages

Before and up to 2017, co-author SAE surveyed and described 69 leaf morphotypes collected from multiple quarries at Blue Rim. As per her (2017b) dissertation, two techniques were used to reconstruct precipitation from foliar assemblages: a univariate approach, leaf area analysis (LAA; Wilf et al., 1998) and a multivariate approach, Climate Leaf Analysis Multivariate Program (CLAMP; Wolfe 1993). LAA is based on the correlation between mean leaf area and annual precipitation, related to transpiration. Leaves with higher surface area to volume ratios transpire more during gas exchange; these larger leaves are typically found in wet areas (Wilf et al., 1998). Leaves in drier climates have smaller leaf area to volume ratios, as they do not have as much plant available water accessible to transpire (Wilf et al., 1998). CLAMP uses 31



morphological characters on at least 20 species of woody “dicots” from any given site to reconstruct eleven aspects of climate, including mean annual precipitation, as well as mean annual temperature (MAT, comparable to mean annual air temperature – MAAT – discussed in this study; Wolfe 1993; Spicer et al., 2009). This method is premised on the relationship between these morphological characters in modern flora and corresponding climate parameters.

230 Physiognomic techniques including CLAMP and leaf margin analysis (LMA; Wilf 1997) were used to calculate mean annual air temperature. LMA uses the correlation between MAAT and the proportion of untoothed to total (untoothed + toothed) species in a local flora (Wolfe 1979; Wilf 1997; Wing & Greenwood 1993; Peppe et al., 2011). See Allen (2017b) for additional reconstruction details based on floral assemblages.

235 3.3.4 Paleoclimate and Paleoenvironmental Reconstructions using Organic and Inorganic Geochemistry

Mean annual precipitation was reconstructed using Chemical Index of Alteration minus potassium (CIA-K; Equation 5; 6; Sheldon et al., 2002; error ± 182 mm yr⁻¹), modified from CIA to control for potassium metasomatism in paleosols (Maynard 1992; Ennis et al., 2000; Sheldon et al., 2002). Mean annual air temperature was calculated using PWI (Equation 7; error of ± 2.1 °C; Gallagher & Sheldon 2013). We applied the empirical relationship between $\delta^{13}\text{C}_{\text{plant}}$ and $\delta^{13}\text{C}_{\text{atm}}$ values found
240 by Arens et al. (2000; Equation 8; $R^2 = 0.34$) and used $\delta^{13}\text{C}_{\text{plant}}$ values of all individual fossils to reconstruct generalized, non-taxon-specific $\delta^{13}\text{C}_{\text{atm}}$ values. We compared this reconstructed value based on a generalized equation with reconstructed values based on species-specific carbon isotope discrimination values (as measured in Cornwell et al., 2018), using fossil *Lygodium* and *Populus* to reconstruct $\delta^{13}\text{C}_{\text{atm}}$ values based on taxon-specific parameters (e.g., Stein et al., 2019; Stein et al., 2021).

245

$$CIA - K = \frac{Al_2O_3}{Al_2O_3 + Na_2O + CaO} * 100 \quad (5)$$

$$MAP = 221e^{0.0197(CIA-K)} \quad (\text{CIA-K for paleosols; 6})$$

$$T (\text{°C})_{PWI} = -2.74 * \ln(PWI) + 21.39 \quad (7)$$

$$\delta^{13}\text{C}_{\text{leaf}} = 1.1 (\delta^{13}\text{C}_{\text{atm}}) + 18.67 \quad (8)$$



250 Holdridge life zones are ecoregions classified by water availability and temperature, that can be further subdivided into successional stages reflecting land use, disturbance history, latitude, altitude (Holdridge 1967; Lugo et al., 1999). The parameters for each life zone are calculated based on potential evapotranspiration and humidity provinces (Holdridge 1967; see Appendix D). Similar metrics that use evapotranspiration and precipitation to quantify ecosystems into “floral humidity provinces” based on paleosol measurements, have been established more recently by Gulbranson et al. (2011; see Appendix
255 D). See supplemental materials for methodology used to determine Holdridge life zones and Floral Humidity Provinces for paleosols (this study) and previously published floras (Leopold & MacGinitie 1972; Roehler 1993; Wing et al., 2005; Smith et al., 2008; Wing & Currano 2013; Allen 2017a/b).

4 Results

260 4.1 Geochronology

Single crystal sanidine $^{40}\text{Ar}/^{39}\text{Ar}$ analyses of four sampled beds yielded ages for the middle and top of the Blue Rim escarpment that are broadly consistent with deposition during the early Eocene (Fig. 1; Table 1; Table S2). Two samples (BR-3 and BR-4) of a horizon containing pumice clasts and biotite grains taken from the base and middle of the ‘blue-green marker’ bed yielded similar coherent young populations of Eocene apparent ages (Figs. 4a; 8a), which are mixed with a
265 subsidiary population of older, presumably detrital or xenocrystic grains (Fig. 8b). Sample BR-3 was collected at the base of the main blue-green marker layer, just above the UF 15761S plant quarry (elevation 2053 m; Allen 2017b), whereas sample BR-4 was collected from the lower part of the blue-green layer in the 2014/UF 19297 stratigraphic section at 2056 m (Allen 2017b). Twenty seven of forty fusions of sanidine from these beds form a coherent population that yields a weighted mean age of 49.29 ± 0.18 Ma (MSWD = 1.08; Table 1), which we interpret to reflect the best estimate of the age of deposition.

270 This age is consistent with the Blue Rim being coeval with Bridger A/1b (Fig. 1).

Single fusions of sanidine from two sand beds (samples BR-5 and BR-6) collected near the top of the escarpment (elevation 2091 m; Allen 2017b) yielded a greater proportion (31 of 38) of older detrital and/or xenocrystic ages than occur in samples of the blue-green marker. Nevertheless, the seven youngest grains from the uppermost sample BR-6 form a coherent population that yields a weighted mean age of 48.48 ± 0.60 Ma (MSWD = 0.60), which can be interpreted to be a



275 maximum depositional age. This imprecise age suggests that the uppermost Blue Rim could be as old as Bridger B/B-2, or as
young as Bridger D/Br-3 (Fig. 1). Altogether, new geochronology indicates that the stratigraphy between the blue-green
marker bed and sand beds likely spans Bridger B, with the uppermost part of the Blue Rim Escarpment being time
equivalent to Bridger C or D/3 (Fig4, 5, 6). This constrains the age of the lower plant horizon to be slightly older than 49.29
Ma (Allen 2017b), whereas the upper plant horizon is likely equivalent to Bridger Br-2. Detrital or xenocrystic grains not
280 included in weighted means discussed above yield a combination of Phanerozoic and Proterozoic apparent ages which are
consistent with detrital feldspar grains sampled from volcanoclastic strata of the Sand Butte bed of the Laney Member (Green
River Formation, Smith et al., 2008; Chetel et al., 2011). The Sand Butte bed forms thick (> 40 m) deltaic foresets that
prograded into and filled Lake Gosiute and parts of Lake Uinta from northwest to southeast (Surdam & Stanley, 1980; Smith
et al., 2008; Chetel & Carroll 2010). These deposits have been hypothesized to represent the inland delta or megafan of the
285 Idaho paleoriver which drained areas as far west as central Idaho (Chetel et al., 2011).

4.2 Paleosol descriptions

Six profiles were sampled laterally from a single paleosol at the base of the Blue Rim escarpment (located at 1 m in
the stratigraphic column; Figs. 4-7). Paleosol profiles (Fig. 7, S1) typically consisted of a silty and/or sandy brown, yellow
290 A-horizon over a parent material C-horizon of green-grey silty mudstone anywhere from ~20 to 112 cm below the surface.
Paleosol #1 was missing a B-horizon due to erosion, while paleosol #4 was missing an A horizon, likely truncated during
burial. Typically, each profile was lighter colored in upper horizons and darker in lower B- and C-horizons. In the paleosol
profiles sampled, every A-horizon but one, and several upper B-horizons, had root traces, kerogenized roots, and/or
rhizoliths. We observed drab-haloed roots in paleosols #1 and 4. Paleosol #2 had vertical burrows of up to 1 cm diameter and
295 ~3 cm length, and paleosol #1 had visible peds (Table S1; Fig. 3a). These soils were well-developed Inceptisols based on
features, textures, and extrapolation from the local flora (Fig. 2a; Fig. S1; S5; Table S1).

4.3 Paleosol geochemistry



On average, the lateral extent of the paleosol found at the base of the Blue Rim stratigraphic section had A-horizon
300 CIA-K values in the 50s with a maximum of ~60 in B- and C- horizons (consistent with expectations for CIA-K values based
on past work; Sheldon et al., 2002; Sheldon & Tabor 2009; Fig. S1b). Ti/Al ratios were constant throughout, ranging from
0.040 to 0.045, typical values of mudstones and sandstone parent materials (Sheldon & Tabor 2009), like those seen in
sediments throughout the Blue Rim escarpment (Fig. S1c; Table S2).

Tau (used to measure mobile element transport) was calculated for soil profiles following Chadwick et al., (1990;
305 Equations 2 and 3) and demonstrated in Supplemental Fig. S2(a-f). Overall, tau values for K, Mg and Na all ranged from 0.0
to -0.5, and tau values for Ca ranged from 0.0 to -1.0, except in paleosol #2 (which was extremely high in Ca), as is typical
for Inceptisols. Tau values for Rb and Fe were generally also between 0.0 and -0.5, though this was less consistent between
profiles. To note, paleosol #1 (19BRWY1; Fig. 7) was excluded for paleoclimate reconstructions due to the lack of presence
of the B- horizon (we identified this soil as an Entisol, which cannot be used for climate reconstructions; see Fig. 7 for
310 location). Paleosol #2 (19BRWY2) was also excluded for climate reconstructions, due to the high % Ca, likely of carbonate
origin as this site was reactive to HCl. Based on both field taxonomy and these geochemical results, paleosols #3-#6 are
identified as Inceptisols.

4.4 Sedimentary geochemistry

315 With a few individual outlier analyses, proxies for leaching intensity (Ba/Sr, and sum bases/Ti; Fig. 4b,c),
hydrolysis (sum bases/Al; Fig. 4d), and measurements of weathering (CIA; Fig. 4e) are consistent throughout the section.
Proxies for provenance also remained nearly constant (Fig. 5a,b) as did proxies for parent material (Fig. 5c,d). Organic
carbon weight percent was high in the same locations throughout the section as CIA, and percent N was low throughout the
section. $\delta^{13}\text{C}_{\text{org}}$ values were most depleted in the sections with highest percent C and N.

320

4.5 Flora

The identifiable fossils from this specific field excursion (2019) sampled specifically for organic isotope analyses
included multiple compression fossils of *Lygodium kaulfussii* (climbing fern, family Lygodiaceae; Manchester & Zavada



1987), as well as one specimen of *Asplenium* sp. (fern, family Aspleniaceae; as described in Allen 2017b), an example of cf.
325 *Populus cinnamomoides* (poplar, family Salicaceae; Manchester et al., 2006), one specimen assigned to cf. *Cedrela*,
(undefined species; mahogany, family Meliaceae; Fig. S5), several dense leaf mats, and assorted twig and branchlet fossils
were recovered. These specimens were collected from the same strata as the lower horizon (e.g., UF 15761N, Allen 2017b),
located 26 m on the stratigraphic column included in this study (Figs. 3–5). There were also fragments of several
unidentified monocots preserved, though no isotope analyses were run on these fossils.

330

4.6 Climate

Mean annual precipitation (MAP) values reconstructed using CIA without potash (CIA-K) on paleosol B-horizons
(Equation 6) ranged from 608–1167 mm yr⁻¹, with an average of 845 mm yr⁻¹ (± 181 mm yr⁻¹; $n = 6$) (Equation 6; Fig. 6;
S6). The lowest estimated MAP value (288 mm yr⁻¹) was excluded due to high % Ca (10.25%) in the B horizon of paleosol
335 2, skewing CIA-K calculations by artificially minimizing the ratio of Al to other metals in the calculation (see Dzombak et
al., in review for discussion of this issue). Mean annual air temperature values (MAAT) reconstructed using PWI on paleosol
B-horizons (Equation 7) ranged from 10.4 to 12.0 °C (± 0.72 °C standard deviation), with an average of 11.0 °C ($n = 6$).

A wide range of $\delta^{13}\text{C}_{\text{atm}}$ values were reconstructed from $\delta^{13}\text{C}_{\text{leaf}}$ from the 34 individual leaf fossils (2019 collection)
using a generalized relationship (Arens et al., 2000). Reconstructions using the generalized Arens et al., (2000) model were
340 done on all 34 individual fossil leaves, even though many of these were unidentified. Additional species-specific tests were
done on all samples of *Lygodium*, cf. *Cedrela* and *Populus* fossils using isotope discrimination values from extant plants of
these genera. Thirty eight percent ($n = 13$) of the 34 $\delta^{13}\text{C}_{\text{atm}}$ values reconstructed using the generalized Arens et al., (2000)
model suggested a $\delta^{13}\text{C}_{\text{atm}}$ value of between -5.32 and -5.82‰. Fifty six percent of these reconstructed values were between -
5.0 and -6.0‰ ($n = 19$; Equation 8; Fig. 9). Limitations on this reconstruction are include species-specific isotopic C isotope
345 discrimination behaviour (Beerling & Royer 2002; Stein et al., 2019; Sheldon et al., 2020), and values outside the range of
most samples (44%) were more extreme potentially preferential diagenesis of certain compounds (Beerling & Royer 2002; Tu
et al., 2004). Using identified *Lygodium*, cf. *Cedrela* and *Populus* fossils ($n = 8$ total), we applied the taxon-specific isotope
discrimination principle and reconstructed an average value of -4.40‰ (minimum value of -5.23‰ and maximum value of -



3.83‰). These reconstructions were based on isotope discrimination values of 19.99‰ for *Lygodium* and 20.05‰ for *Populus*
350 (as reported in modern isotope analyses by Cornwell et al., 2018).

5 Discussion

5.1 Geochronology

The new $^{40}\text{Ar}/^{39}\text{Ar}$ dates presented here for the blue-green marker bed and sand beds above the floral quarries suggest
355 that the Blue Rim section likely spans ca. 49.5 to 48.5 Ma, making it slightly younger than the EECO. Assuming constant
sedimentation rates based on a linear interpolation between ages of 1 m per ~23 ka (or ~44 $\mu\text{m yr}^{-1}$, slightly slower than
accumulation rates of 65 $\mu\text{m yr}^{-1} \pm 19/-12$ in the Laney Member below (e.g., Smith et al., 2010), the newly described paleosols
are roughly 684,300 years older than the blue-green marker bed, or 49.97 Ma. The Wilkins Peak Member, and part of the
Laney Member of the Green River Formation underlie the Blue Rim strata; thus, the approximate age for the paleosols based
360 on constant sedimentation rate is consistent with Blue Rim being younger than ~50 Ma, when the Wilkins Peak Member
transitioned to the Laney Member (Smith et al., 2015; see Fig. 1).

5.2 Stratigraphy, provenance, and weathering

Detrital feldspar geochronology and geochemistry strongly suggest that provenance remained constant throughout
365 accumulation of the stratigraphic section, which can be interpreted to mean that the material did not systemically change
across deposition, and geochemical proxies used to reconstruct climate are not affected by provenance shifts. A sudden 6 ‰
decrease in $\delta^{18}\text{O}$ was previously observed in sections of the Green River Formation, and it was hypothesized that this could
be due to a sudden change in river capture to include a river with isotopically depleted waters from different headwaters
(Doebbert et al., 2010). With new river catchments, there is a potential change in sedimentological inputs that could
370 overwrite climate signals, so these geochemical proxies provide assurance that the climate interpretations based on
geochemical proxies are not actually changes in allochthonous materials. Assumptions about provenance were supported by
parent material data, which showed that all sources were primarily sedimentary. The consistent Ti/Al, U/Th, and La/Ce
ratios correspond to constant parent material throughout the one million years section covered by the Blue Rim stratigraphic



column, demonstrating that basin-scale hydrology was likely not reorganized during this time. The one exception to constant
375 parent material and provenance ratios is the anomalously high U/Th ratio in the blue-green marker bed (0.87). This proxy is
redox-sensitive, so this anomalously high U/Th ratio is due to the preferential redistribution and accumulation of U in this
section, as Th is insoluble and immobile (Pett-Ridge et al., 2007; Sheldon & Tabor 2009). Weathering and leaching were
highest in the sections where there was high carbon content; this correlation is likely due to organic acids produced by plants
in the ecosystem that contribute to chemical weathering (Fig. S4; $R^2 = 0.20$; p -value = 0.01; Ong et al., 1970; Berner 1992).

380

5.3 Global and regional climate

Generally, the early Eocene of North America had widespread temperate to subtropical wet forests due to global
warmer, wetter conditions (Leopold & MacGinitie 1972; Wing & Greenwood 1993; Greenwood & Wing 1995; Inglis et al.,
2017; Murphey et al., 2017). Depending on latitude of site, other studies indicate slightly warmer conditions temperature
385 reconstructions from Blue Rim (Allen 2017a/b). Generally, mean annual air temperatures reconstructed from other mid to
high- latitude sites between 36 and 80 °N have ranges from 35°C (36 °N) to 8°C (80 °N; using leaf margin analyses and oxygen
isotopes; Fricke & Wing 2004).

More locally, temperature reconstructions of other Wyoming formations based on floral assemblages from earlier in
the Eocene were higher than paleosol-based reconstructions at Blue Rim (i.e., paleosol-based estimates were 12 °C, while
390 other temperature reconstructions were higher; Wilf 2000, Wing et al., 2005; Hyland et al., 2018; Fig. 11), though
contemporaneous plant-based reconstructions were more comparable ~12 °C (Leopold & MacGinitie 1972; Allen 2017b; Fig.
11). Summer months were warm, and winter months mild, with temperatures from 18 to 34 °C and 4 to 7 °C respectively
(based on Δ_{47} ; Kelson et al., 2017; Hyland et al., 2018).

The location of Blue Rim appears to have been a “wet forest” at the time of deposition, as calculated from
395 temperature and precipitation estimates from paleosols and using leaf physiognomic techniques (see supplemental methods
for details; Fig. 10). The paleosol-based results are within error of flora-only estimates based on contemporaneous Blue Rim
reconstructions by Allen (2017b) and Wilf et al., (2000; other southwest Wyoming localities including Little Mountain,
Niland Tongue, Sourdough, Latham, Wasatch Main Body, Big Multi Quarry, and Bison Basin) as well as Wing et al.’s



(2005) ecosystem reconstruction of the Paleocene-Eocene thermal maximum (PETM; Bighorn Basin in north-central
400 Wyoming; Fig. 11; Fig. S7). Indeed, fossils collected for organic analysis at Blue Rim escarpment included mineralized
trunks and fern and angiosperm leaf macrofossils including: *Lygodium kaulfussii*, *Asplenium*, *Populus cinnamomoides*, cf.
Cedrela, as well as dense leaf mats. These collected fossils (sampled at 26 m on the stratigraphic section and housed at ESS
laboratory at the University of Michigan) are comparable to fossils found by Allen (2017b; Bridger Formation) and
MacGinitie (1969; Green River Formation) and are characteristic of mesic, forested environment (e.g., wet forest; Hamzeh &
405 Dayanandan 2004; Hamzeh et al., 2006).

While the leaf physiognomic and paleosol-based estimates are modestly different, we cannot differentiate between
whether there was a slight increase in both MAAT and MAP or whether climate was steady for the entirety of the record at
Blue Rim, because calculated values were within error. One possible explanation for the slight discrepancy between leaf
physiognomic and soil-based temperature reconstructions at Blue Rim could be related to the soil taxonomy; the PWI tool
410 used to reconstruct temperature was calibrated for Inceptisols, Alfisols and Ultisols. However, none of the Inceptisols
sampled to create this proxy were from mean annual air temperatures >12 °C because for the most part, Inceptisols are
relatively uncommon in areas warmer than that at modern (Gallagher & Sheldon 2013). Because the early Eocene was
significantly warmer, it is possible that early developmental soils like Inceptisols existed at higher temperatures, especially in
dynamic ecosystems with frequent flooding events like those preserved at the Blue Rim escarpment, and that temperature
415 reconstructions based on PWI for these Inceptisols are underestimates.

Leaf physiognomic proxies could contribute to the discrepancy as well; CLAMP has been cited as often producing
overestimates of precipitation (Wilf et al., 1998; Allen 2017b). This is exacerbated when there are fewer than 25
morphotypes available, which was the case at Blue Rim (Wolfe 1993; Spicer et al., 2009; Allen 2017b). CLAMP estimates
may be less accurate due to the threshold number of morphotypes used at Blue Rim escarpment (20); the number of
420 morphotypes used for CLAMP temperature reconstructions was exactly the minimum recommended value (Allen 2017b).

Regardless of the cause of discrepancy or if it represents modest actual change versus stasis, this study demonstrates
the importance of the holistic approach that combines both types of proxies. However, based upon their close statistical



agreement (Figure 6) and implications for the overall ecosystem (Figure 10), we interpret the overall climate as relatively steady during this interval.

425

5.4 Maintaining Warmth in the Paleogene

The maintenance of extended warmth and elevated CO₂ during the early Eocene is debated (Hyland & Sheldon 2013), which emphasizes the importance of $\delta^{13}\text{C}_{\text{atm}}$ values that can constrain CO₂ sources. Some scientists invoke the destabilization of deep-sea methane hydrates as the mechanism for CO₂ increase, while others pinpoint volcanic emissions (Reagan et al., 2013) and reduced silica weathering (Zachos et al., 2008; Lunt et al., 2011). These mechanisms occur on very different timescales (e.g., methane has a lifetime of 12 years in the atmosphere; Schiermeier 2020), and thus require vastly different environmental processes and landscapes. It is possible to determine the source of atmospheric CO₂ by examining the isotopic signature of the atmosphere; volcanic CO₂ has an isotopic composition of -5.4 ‰ (Deines 1992) while methane hydrates are far more depleted (e.g., -64.5 to -67.5 ‰ off the coast of central Oregon; Kastner et al., 1998). As mentioned above, based on the comparative Arens et al., (2000) model, $\delta^{13}\text{C}_{\text{leaf}}$ values can be used to infer $\delta^{13}\text{C}_{\text{atm}}$ values. These values are also important parameters in models that reconstruct additional environmental variables, such as the concentration of atmospheric CO₂ using paleosol carbonates (Cerling et al., 1991; Cerling 1992) or using stomatal parameters (Franks et al., 2014). Our large sample size of distinguishable leaf fossils from a single horizon ($n = 34$) allowed us to statistically determine the most likely $\delta^{13}\text{C}_{\text{atm}}$ value based on the general relationship proposed by Arens et al., (2000) to be between -5.32 and -5.82‰. Analyses with taxon-specific reconstructions ($n = 9$ total specimens of these genera: *Lygodium*, cf. *Cedrela* and *Populus* fossils), using extant members of these genera to determine isotope discrimination and reconstruct the atmosphere (as published in Cornwell et al., 2018) had an average value of -4.82‰ ($\pm 0.92\%$ standard deviation). Both generalized and taxon-specific reconstructions were within error of the isotopic value of mantle CO₂ (-5.4‰; Deines 1992), and comparable to the value reconstructed for ~49 Ma using benthic and planktonic foraminifera, -5.4‰ (Tippie et al., 2010). Although we cannot rule out short term perturbations of other C pools (e.g., methane hydrates during the PETM, Foster et al., 2018), these results point to a long-term volcanic source of CO₂ that drove long-term warmth in the Paleogene.

445



This period of elevated rates of volcanism slowed as global CO₂ and temperatures dropped at the Eocene-Oligocene transition (EOT; see Zachos et al., 2008; Fig. 11), and likely included Challis volcanics locally (Fig. 3a; Chetel et al., 2011).

450 6 Conclusions

The age findings contained in this study constrain the time for the Blue Rim wet forests to be slightly younger than previous estimates, with the upper half of the section clearly deposited after the EECO. Based on dating and sedimentation rates, the lower part of the section could overlap with the end of the EECO, but there is an absence of observable changes in proxy records. During the EECO, the Blue Rim escarpment received between 608–1167 mm yr⁻¹ of precipitation, likely
455 related to different moisture regimes, and was a productive paratropical (non-equatorial tropical) forest. Although reconstructed temperature and precipitation values using paleosol and sedimentary geochemistry are lower than published values reconstructed from flora, the values from all of the proxies all fall within error of one another (see supplemental materials). Furthermore, the Holdridge life zones and floral humidity provinces calculated for both leaf physiognomic-based and geochemistry-based reconstructions are comparable, pinpointing this region as a warm, wet forest at ~49 Ma.

460 The new age constraints, evidence from leaf fossils, and inorganic and organic geochemical proxies at Blue Rim escarpment make it possible to reconstruct the depositional environment of the central region of Lake Gosiute in an unprecedented way. The consistent Ti/Al, U/Th, and La/Ce ratios to determine provenance and parent material throughout the Blue Rim stratigraphic column demonstrate that the hydrological and sedimentological inputs remained stable for this location throughout the ~one million years spanned by this section. The use of multiple proxies to cross-compare sites is
465 under-utilized in paleoclimate reconstructions but allows for an improved understanding of regional and more broad-scale climate regimes. Based on ample floral and geochemical data, ~49.5 to 48.5 million years ago – after the peak of the EECO – southwest Wyoming was a warm, wet forest atop deltaic deposition (Fig. 3a; Chetel et al., 2011) with little to no frost and mild temperatures, in agreement with previous work based only on fossil floras (e.g., MacGinitie 1969; Wilf 2000) or paleosols (Hyland et al., 2018) individually.

470

7 Author contributions



NDS and RAS conceived and designed the study. RMD and RAS collected the data in the field. MES, SEA and BRJ contributed data. NDS and MES were responsible for funding acquisition, and RAS acquired funding for field work. NDS was responsible for project administration, provision of resources and supervision to RAS. RAS was primarily responsible for the investigation and performed many of the visualizations. RMD, MES, and SEA contributed visualizations as well. RAS and NDS were responsible for the original draft, and all authors were responsible for review and editing.

8 Acknowledgments

We thank Nikolas C. Midttun for assistance measuring, creating, and sampling the stratigraphic column at the Blue Rim escarpment in June 2019. We thank Steven R. Manchester for personal communications regarding the location of floral fossil quarries at Blue Rim. We thank Selena Y. Smith for personal communications and consultation regarding fossils and for access to her camera and camera stand for fossil photographs. We acknowledge Naomi E. Levin, Christopher J. Poulsen and Gretchen Keppel-Aleks for their feedback on this manuscript. This work was partially funded by NSF Award #1812949 to Nathan Sheldon and Michael Smith, and an Evolving Earth Graduate Research Grant to RAS. The geochemical dataset for this manuscript can be found at Mendeley Data Repository under the title “Blue Rim escarpment geochemical data”, Mendeley Data, V1, doi: 10.17632/z6twpstz4r.1.

References

- Allen, S.E., (2015). Fossil palm flowers from the Eocene of the Rocky Mountain region with affinities to *Phoenix* L. (Arecaceae: Coryphoideae). *International Journal of Plant Sciences*, 176, 586-596.
- Allen, S.E., Stull, G. W. & Manchester, S. R. (2015). Icacinaeae from the Eocene of western North America. *American Journal of Botany*, 102, 725-744.
- Allen, S. E. (2017a). Reconstructing the local vegetation and seasonality of the Lower Eocene Blue Rim site of southwestern Wyoming using fossil wood. *International Journal of Plant Sciences*, 178(9), 689-714.
- Allen, S. E. (2017b). The Uppermost Lower Eocene Blue Rim Flora from the Bridger Formation of Southwestern Wyoming: Floristic Composition, Paleoclimate, and Paleoecology. Doctoral Dissertation, University of Florida.
- Anagnostou, E., John, E. H., Edgar, K. M., Foster, G. L., Ridgwell, A., Inglis, G. N., Pancost, R. D., Lunt, D. J. & Pearson, P. N. (2016). Changing atmospheric CO₂ concentration was the primary driver of early Cenozoic climate. *Nature*, 533(7603), 380-384.



- 500 Arens, N. C., Jahren, A. H., & Amundson, R. (2000). Can C₃ plants faithfully record the carbon isotopic composition of atmospheric carbon dioxide? *Paleobiology*, 26(1), 137-164.
- Barclay, R. S., & Wing, S. L. (2016). Improving the Ginkgo CO₂ barometer: implications for the early Cenozoic atmosphere. *Earth and Planetary Science Letters*, 439, 158-171.
- Beerling, D. J., & Royer, D. L. (2002). Fossil plants as indicators of the Phanerozoic global carbon cycle. *Annual Review of Earth and Planetary Sciences*, 30(1), 527-556.
- 505 Berner, R. A. (1992). Weathering, plants, and the long-term carbon cycle. *Geochimica et Cosmochimica Acta*, 56(8), 3225-3231.
- Bestland, E. A. (2000). Weathering flux and CO₂ consumption determined from paleosol sequences across the Eocene–Oligocene transition. *Palaeogeography, Palaeoclimatology, Palaeoecology*, 156(3-4), 301-326.
- 510 Bijl, P. K., Houben, A. J., Schouten, S., Bohaty, S. M., Sluijs, A., Reichert, G. J., Damsté, J. S. S. & Brinkhuis, H. (2010). Transient Middle Eocene atmospheric CO₂ and temperature variations. *Science*, 330(6005), 819-821.
- Boutton, T. W. (1991). Stable Carbon Isotope Ratios of Natural Materials: I. Sample Preparation and Mass Spectrometric. Carbon isotope techniques, 1, 155.
- Brand, L. R., Goodwin, H. T., Ambrose, P. D., & Buchheim, H. P. (2000). Taphonomy of turtles in the middle Eocene Bridger Formation, SW Wyoming. *Palaeogeography, Palaeoclimatology, Palaeoecology*, 162(1-2), 171-189.
- 515 Breedlovestrout, R. L., Evraets, B. J., and Parrish, J. T. (2013). New Paleogene climate analysis of western Washington using physiognomic characteristics of fossil leaves, *Palaeogeography Palaeoclimatology, Palaeoecology*, 392, 22–40.
- Buchheim, H. P., Brand, L. R., & Goodwin, H. T. (2000). Lacustrine to fluvial floodplain deposition in the Eocene Bridger Formation. *Palaeogeography, Palaeoclimatology, Palaeoecology*, 162(1-2), 191-209.
- 520 Cerling, T. E., Solomon, D. K., Quade, J. A. Y., & Bowman, J. R. (1991). On the isotopic composition of carbon in soil carbon dioxide. *Geochimica et Cosmochimica Acta*, 55(11), 3403-3405.
- Cerling, T. E. (1992). Use of carbon isotopes in paleosols as an indicator of the P(CO₂) of the paleoatmosphere. *Global Biogeochemical Cycles*, 6(3), 307-314.
- Cheeseman, J. (2016). Food security in the face of salinity, drought, climate change, and population growth. In *Halophytes for food security in dry lands* (pp. 111-123). Academic Press.
- 525 Chetel, L. M., & Carroll, A. R. (2010). Terminal infill of Eocene Lake Gosiute, Wyoming, USA. *Journal of Sedimentary Research*, 80(6), 492-514.
- Chetel, L. M., Janecke, S. U., Carroll, A. R., Beard, B. L., Johnson, C. M., & Singer, B. S. (2011). Paleogeographic reconstruction of the Eocene Idaho River, North American Cordillera. *GSA Bulletin*, 123(1-2), 71-88.
- 530 Clyde, W. C., Sheldon, N. D., Koch, P. L., Gunnell, G. F., & Bartels, W. S. (2001). Linking the Wasatchian/Bridgerian boundary to the Cenozoic Global Climate Optimum: new magnetostratigraphic and isotopic results from South Pass, Wyoming. *Palaeogeography, Palaeoclimatology, Palaeoecology*, 167(1-2), 175-199.



- Cotton, J. M., Jeffery, M. L., & Sheldon, N. D. (2013). Climate controls on soil respired CO₂ in the United States: implications for 21st century chemical weathering rates in temperate and arid ecosystems. *Chemical Geology*, 358, 37-45.
- 535 Cornwell, W. K., Wright, I. J., Turner, J., Maire, V., Barbour, M. M., Cernusak, L. A., Dawson, T., Ellsworth, D., Farquhar, G. D., Griffiths, H. & Keitel, C. (2018). Climate and soils together regulate photosynthetic carbon isotope discrimination within C₃ plants worldwide. *Global Ecology and Biogeography*, 27(9), 1056-1067.
- Deines, P. (1992). Mantle carbon: concentration, mode of occurrence, and isotopic composition. In *Early Organic Evolution* (pp. 133-146). Springer, Berlin, Heidelberg.
- 540 Dickinson, W. R., Klute, M. A., Hayes, M. J., Janecke, S. U., Lundin, E. R., McKittrick, M. A., & Olivares, M. D. (1988). Paleogeographic and paleotectonic setting of Laramide sedimentary basins in the central Rocky Mountain region. *Geological Society of America Bulletin*, 100(7), 1023-1039.
- Dillhoff, R. M., Dillhoff, T. A., Greenwood, D. R., DeVore, M. L., & Pigg, K. B. (2013). The Eocene Thomas Ranch flora, Allenby Formation, Princeton, British Columbia, Canada. *Botany*, 91(8), 514-529.
- 545 Doebbert, A. C., Carroll, A. R., Mulch, A., Chetel, L. M., & Chamberlain, C. P. (2010). Geomorphic controls on lacustrine isotopic compositions: evidence from the Laney Member, Green River Formation, Wyoming. *GSA Bulletin*, 122(1-2), 236-252.
- Dzombak, R. M., Sheldon, N. D., Mohabey, D. M., & Samant, B. (2020). Stable climate in India during Deccan volcanism suggests limited influence on K–Pg extinction. *Gondwana Research*, 85, 19-31.
- 550 Dzombak, R. M., Midttun, Nikolas C., Stein, R. A., & Sheldon, N. D. (in review). Incorporating lateral variability and extent of paleosols into proxy uncertainty. *Submitted to Palaeogeography, Palaeoclimatology, Palaeoecology*.
- Ekart, D. D., Cerling, T. E., Montanez, I. P., & Tabor, N. J. (1999). A 400-million-year carbon isotope record of pedogenic carbonate: implications for paleoatmospheric carbon dioxide. *American Journal of Science*, 299(10), 805-827.
- Ennis, D. J., Dunbar, N. W., Campbell, A. R., & Chapin, C. E. (2000). The effects of K-metasomatism on the mineralogy and geochemistry of silicic ignimbrites near Socorro, New Mexico. *Chemical Geology*, 167(3-4), 285-312.
- 555 Fletcher, B. J., Brentnall, S. J., Anderson, C. W., Berner, R. A., & Beerling, D. J. (2008). Atmospheric carbon dioxide linked with Mesozoic and early Cenozoic climate change. *Nature Geoscience*, 1(1), 43.
- Foster, G. L., Hull, P., Lunt, D. J., & Zachos, J. C. (2018). Placing our current ‘hyperthermal’ in the context of rapid climate change in our geological past. *Philosophical Transactions of the Royal Society A*, 376(2130), 20170086.
- 560 Franks, P. J., & Beerling, D. J. (2009). CO₂-forced evolution of plant gas exchange capacity and water-use efficiency over the Phanerozoic. *Geobiology*, 7(2), 227-236.
- Franks, P. J., Royer, D. L., Beerling, D. J., Van de Water, P. K., Cantrill, D. J., Barbour, M. M., & Berry, J. A. (2014). New constraints on atmospheric CO₂ concentration for the Phanerozoic. *Geophysical Research Letters*, 41(13), 4685-4694.
- 565 Fricke, H. C., & Wing, S. L. (2004). Oxygen isotope and paleobotanical estimates of temperature and δ¹⁸O–latitude gradients over North America during the early Eocene. *American Journal of Science*, 304(7), 612-635.



- Gallagher, T. M., & Sheldon, N. D. (2013). A new paleothermometer for forest paleosols and its implications for Cenozoic climate. *Geology*, 41(6), 647-650.
- 570 Gingerich, P. D. (2003). Mammalian responses to climate change at the Paleocene-Eocene boundary: Polecat Bench record in the northern Bighorn Basin, Wyoming. In S.L. Wing, P.D. Gingerich, B. Schmitz, & E. Thomas (Eds.), *Causes and Consequences of Globally Warm Climates in the Early Paleogene*, (Geological Society of America Special Paper 369, 463-478.
- Greenwood, D. R., & Wing, S. L. (1995). Eocene continental climates and latitudinal temperature gradients. *Geology*, 23(11), 1044-1048.
- 575 Greenwood, D. R., Scarr, M. J., & Christophel, D. C. (2003). Leaf stomatal frequency in the Australian tropical rainforest tree *Neolitsea dealbata* (Lauraceae) as a proxy measure of atmospheric pCO₂. *Palaeogeography, Palaeoclimatology, Palaeoecology*, 196(3-4), 375-393.
- Greenwood, D. R., Archibald, S. B., Mathewes, R. W., & Moss, P. T. (2005). Fossil biotas from the Okanagan Highlands, southern British Columbia and northeastern Washington State: climates and ecosystems across an Eocene landscape. *Canadian Journal of Earth Sciences*, 42(2), 167-185.
- 580 Greenwood, D. R., Pigg, K. B., Basinger, J. F., and DeVore, M. L. (2016). A review of paleobotanical studies of the Early Eocene Okanagan (Okanogan) Highlands floras of British Columbia, Canada and Washington, USA, *Canadian Journal of Earth Sciences*, 53, 548–564, <https://doi.org/10.1139/cjes-2015-0177>.
- Gregory-Wodzicki, K. M. (1997). The Late Eocene House Ranch Flora, Sevier Desert, Utah: Paleoclimate and Paleoelevation. *Palaios*, 12, 552-567.
- 585 Grein, M., Konrad, W., Wilde, V., Utescher, T., & Roth-Nebelsick, A. (2011). Reconstruction of atmospheric CO₂ during the early middle Eocene by application of a gas exchange model to fossil plants from the Messel Formation, Germany. *Palaeogeography, Palaeoclimatology, Palaeoecology*, 309(3-4), 383-391.
- Groll, P. E., & Steidtmann, J. R. (1987). Fluvial response to Eocene tectonism, the Bridger Formation, southern Wind River Range, Wyoming, *Recent Developments in Fluvial Sedimentology*, SP39, 1987.
- 590 Gulbranson, E. L., Montanez, I. P., & Tabor, N. J. (2011). A proxy for humidity and floral province from paleosols. *The Journal of Geology*, 119(6), 559-573.
- Hamzeh, M., & Dayanandan, S. (2004). Phylogeny of *Populus* (Salicaceae) based on nucleotide sequences of chloroplast TRNT-TRNF region and nuclear rDNA. *American Journal of Botany*, 91(9), 1398-1408.
- 595 Hamzeh, M., Périnet, P., & Dayanandan, S. (2006). Genetic Relationships among species of *Populus* (Salicaceae) based on nuclear genomic data. *The Journal of the Torrey Botanical Society*, 133(4), 519-527.
- Haynes, S. J., MacLeod, K. G., Ladant, J. B., Guchte, A. V., Rostami, M. A., Poulsen, C. J., & Martin, E. E. (2020). Constraining sources and relative flow rates of bottom waters in the Late Cretaceous Pacific Ocean. *Geology*, 48(5), 509-513.
- 600 Henehan, M. J., Ridgwell, A., Thomas, E., Zhang, S., Alegret, L., Schmidt, D. N., Rae, J. W., Witts, J. D., Landman, N. H., Green, S. E., & Huber, B. T. (2019). Rapid ocean acidification and protracted Earth system recovery followed the end-Cretaceous Chicxulub impact. *Proceedings of the National Academy of Sciences*, 116(45), 22500-22504.



- Henehan, M., Edgar, K., Foster, G., Oenman, D., Hull, P., Greenop, R., Anagnostou, E., & Pearson, P. (2020). Revisiting the Middle Eocene Climatic Optimum ‘Carbon Cycle Conundrum’ with new estimates of atmospheric pCO₂ from boron isotopes. *Paleoceanography and Paleoclimatology*, 35(6)
- 605 Holdridge, L. R. (1967). *Life Zone Ecology*. Tropical Science Center, San Jose, Costa Rica. (rev. ed.), 1-206.
- Huang, C., Retallack, G.J., Wang, C., & Huang, Q. (2013). Paleatmospheric pCO₂ fluctuations across the Cretaceous–Tertiary boundary recorded from paleosol carbonates in NE China. *Palaeogeography, Palaeoclimatology, Palaeoecology*, 385, 95-105.
- 610 Hyland, E. G., & Sheldon, N. D. (2013). Coupled CO₂-climate response during the early Eocene climatic optimum. *Palaeogeography, Palaeoclimatology, Palaeoecology*, 369, 125-135.
- Hyland, E., Sheldon, N. D., & Fan, M. (2013). Terrestrial paleoenvironmental reconstructions indicate transient peak warming during the early Eocene climatic optimum. *GSA Bulletin*, 125(7-8), 1338-1348.
- Hyland, E. G., Huntington, K. W., Sheldon, N. D., & Reichgelt, T. (2018). Temperature seasonality in the North American continental interior during the Early Eocene Climatic Optimum. *Climates of the Past*, 14, 1391-1404.
- 615 Inglis, G. N., Collinson, M. E., Riegel, W., Wilde, V., Farnsworth, A., Lunt, D. J., ... & Pancost, R. D. (2017). Mid-latitude continental temperatures through the early Eocene in western Europe. *Earth and Planetary Science Letters*, 460, 86-96.
- Jacobs, B. F. (2004). Palaeobotanical studies from tropical Africa: relevance to the evolution of forest, woodland and savannah biomes. *Philosophical Transactions of the Royal Society of London, B, Biological Sciences*, 359, 1573-1583.
- 620 Jagniecki, E. A., Lowenstein, T. K., Jenkins, D. M., & Demicco, R. V. (2015). Eocene atmospheric CO₂ from the nahcolite proxy. *Geology*, 43(12), 1075-1078.
- Jicha, B. R., & Brown, F. H. (2014). An age for the Korath Range, Ethiopia and the viability of 40Ar/39Ar dating of kaersutite in Late Pleistocene volcanics. *Quaternary Geochronology*, 21, 53-57.
- 625 Kastner, M., Kvenvolden, K. A., & Lorenson, T. D. (1998). Chemistry, isotopic composition, and origin of a methane-hydrogen sulfide hydrate at the Cascadia subduction zone. *Earth and Planetary Science Letters*, 156(3-4), 173-183.
- Keeling, C. D., MOOK, W. G., & Tans, P. P. (1979). Recent trends in the ¹³C/¹²C ratio of atmospheric carbon dioxide. *Nature*, 277(5692), 121-123.
- 630 Kelson, J. R., Huntington, K. W., Schauer, A. J., Saenger, C., & Lechler, A. R. (2017). Toward a universal carbonate clumped isotope calibration: Diverse synthesis and preparatory methods suggest a single temperature relationship. *Geochimica et Cosmochimica Acta*, 197, 104-131.
- Kistner, F. B. (1973). Stratigraphy of the Bridger Formation in the Big Island-Blue Rim area, Sweetwater County, Wyoming. [Masters’ Thesis], University of Wyoming, Laramie, Wyoming.
- Koenig, K. J. (1960). Bridger Formation in the Bridger Basin, Wyoming. *Overthrust Belt of Southwestern Wyoming and Adjacent Areas; 15th Annual Field Conference Guidebook*, 163-168.



- 635 Kowalczyk, J. B., Royer, D. L., Miller, I. M., Anderson, C. W., Beerling, D. J., Franks, P. J., Grein, M., Konrad, W., Roth-Nebelsick, A., Bowring, S. A., & Johnson, K. R. (2018). Multiple proxy estimates of atmospheric CO₂ from an early Paleocene rainforest. *Paleoceanography and Paleoclimatology*, 33(12), 1427-1438.
- Kowalski, E. A., & Dilcher, D. L. (2003). Warmer paleotemperatures for terrestrial ecosystems. *Proceedings of the National Academy of Sciences*, 100(1), 167-170.
- 640 Kuiper, K.F.A., Deino, F.J.K., Hilgen, W., Renne, P.R., Wijbrans, J.R. (2008). Synchronizing rock clocks of Earth history. *Science* 320: 500-504.
- Leopold, E. B., & MacGinitie, H. D. (1972). Development and affinities of Tertiary floras in the Rocky Mountains. In A. Graham (Ed.), *Floristics and Paleoflorists of Asia and Eastern North America*. (pp. 147-200). Elsevier Publishing Company.
- 645 Liu, X. Y., Gao, Q., Han, M., & Jin, J. H. (2016). Estimates of late middle Eocene pCO₂ based on stomatal density of modern and fossil *Nageia* leaves. *Climate of the Past*, 12, 241-253.
- Looy, C., Kerp, H., Duijnste, I., & DiMichele, B. (2014). The late Paleozoic ecological-evolutionary laboratory, a land-plant fossil record perspective. *The Sedimentary Record*, 12(4), 4-18.
- Lowenstein, T. K., & Demicco, R. V. (2006). Elevated Eocene atmospheric CO₂ and its subsequent decline. *Science*, 313(5795), 1928-1928.
- 650 Lugo, A. E., Brown, S. L., Dodson, R., Smith, T. S., & Shugart, H. H. (1999). The Holdridge life zones of the conterminous United States in relation to ecosystem mapping. *Journal of Biogeography*, 26(5), 1025-1038.
- Lunt, D. J., Ridgwell, A., Sluijs, A., Zachos, J., Hunter, S., & Haywood, A. (2011). A model for orbital pacing of methane hydrate destabilization during the Palaeogene. *Nature Geoscience*, 4(11), 775-778.
- 655 MacGinitie, H. D. (1969). *The Eocene Green River flora of northwestern Colorado and northeastern Utah*. University of California Press.
- Manchester, S. R., & Zavada, M. S. (1987). *Lygodium* foliage with intact sorophores from the Eocene of Wyoming. *Botanical Gazette*, 148(3), 392-399.
- Manchester, S. R., Judd, W. S., & Handley, B. (2006). Foliage and fruits of early poplars (Salicaceae: *Populus*) from the Eocene of Utah, Colorado, and Wyoming. *International Journal of Plant Sciences*, 167(4), 897-908.
- 660 Matthew, W. D. (1909). *The Carnivora and Insectivora of the Bridger basin, middle Eocene*. EW Wheeler, printer.
- Maxbauer, D. P., Royer, D. L., & LePage, B. A. (2014). High Arctic forests during the middle Eocene supported by moderate levels of atmospheric CO₂. *Geology*, 42(12), 1027-1030.
- 665 Maynard, J. B. (1992). Chemistry of modern soils as a guide to interpreting Precambrian paleosols. *The Journal of Geology*, 100(3), 279-289.
- McElwain, J. C. (1998). Do fossil plants signal palaeoatmospheric carbon dioxide concentration in the geological past?. *Philosophical Transactions of the Royal Society of London. Series B: Biological Sciences*, 353(1365), 83-96.



- Miller, I. M., Brandon, M. T., & Hickey, L. J. (2006). Using leaf margin analysis to estimate the mid-Cretaceous (Albian) paleolatitude of the Baja BC block. *Earth and Planetary Science Letters*, 245(1-2), 95-114.
- 670 Milligan, J. N., Royer, D. L., Franks, P. J., Upchurch, G. R., & McKee, M. L. (2019). No evidence for a large atmospheric CO₂ spike across the Cretaceous-Paleogene boundary. *Geophysical Research Letters*, 46(6), 3462-3472.
- Min, K., Mundil, R., Renne, P. R., & Ludwig, K. R. (2000). A test for systematic errors in ⁴⁰Ar/³⁹Ar geochronology through comparison with U/Pb analysis of a 1.1-Ga rhyolite. *Geochimica et Cosmochimica Acta*, 64(1), 73-98.
- 675 Murphey, P. C., & Evanoff, E. (2001). Stratigraphy, fossil distribution, and depositional environments of the upper Bridger Formation (Middle Eocene), Southwestern Wyoming. *Wyoming State Geological Survey*.
- Murphey, P. C., Torick, L. L., Bray, E. S., Chandler, R., & Evanoff, E. (2001). Taphonomy, fauna, and depositional environment of the *Omomys* Quarry, an unusual accumulation from the Bridger Formation (middle Eocene) of Southwestern Wyoming (USA). In *Eocene Biodiversity* (pp. 361-402). Springer, Boston, MA.
- 680 Murphey, P. C., & Evanoff, E. (2007). Stratigraphy. *Fossil Distribution and Depositional Environments of the Upper Bridger Formation (Middle Eocene), Southwestern Wyoming: Wyoming State Geological Survey Report of Investigations*, 57.
- Murphey, P. C., & Evanoff, E. M. M. E. T. T. (2011). Paleontology and stratigraphy of the middle Eocene Bridger Formation, southern Green River basin, Wyoming. In *Proceedings of the Ninth Conference on Fossil Resources: Brigham Young University Geology Studies*, 49, 83-109.
- 685 Murphey, P., Townsend, K. E., Friscia, A., Westgate, J., Evanoff, E., & Gunnell, G. (2017). Paleontology and stratigraphy of Middle Eocene rock units in the southern Green River and Uinta Basins, Wyoming and Utah. *Geology of the Intermountain West*, 4, 1-53.
- Nesbitt, H., & Young, G. M. (1982). Early Proterozoic climates and plate motions inferred from major element chemistry of lutites. *Nature*, 299(5885), 715-717.
- 690 Ong, H. L., Swanson, V. E., & Bisque, R. E. (1970). Natural organic acids as agents of chemical weathering. *Geological Survey Research, Paper*.
- Osborn, H.F. (1909). Cenozoic mammal horizons of western North America. *U.S. Geological Survey Bulletin*, 361, 1-138.
- Pagani, M., Zachos, J. C., Freeman, K. H., Tipler, B., & Bohaty, S. (2005). Marked decline in atmospheric carbon dioxide concentrations during the Paleogene. *Science*, 309(5734), 600-603.
- 695 Pagani, M., Huber, M., Liu, Z., Bohaty, S. M., Henderiks, J., Sijp, W., ... & DeConto, R. M. (2011). The role of carbon dioxide during the onset of Antarctic glaciation. *Science*, 334(6060), 1261-1264.
- Passchier, S., Bohaty, S. M., Jiménez-Espejo, F., Pross, J., Röhl, U., van de Flierdt, T., Escutia, C., & Brinkhuis, H. (2013). Early Eocene to middle Miocene cooling and aridification of East Antarctica. *Geochemistry, Geophysics, Geosystems*, 14(5), 1399-1410.
- 700 Pearson, P. N., & Palmer, M. R. (2000). Atmospheric carbon dioxide concentrations over the past 60 million years. *Nature*, 406(6797), 695-699.
- Peppe, D. J., Royer, D. L., Cariglino, B., Oliver, S. Y., Newman, S., Leight, E., ... & Correa, E. (2011). Sensitivity of leaf size and shape to climate: global patterns and paleoclimatic applications. *New phytologist*, 190(3), 724-739.



- 705 Pett-Ridge, J. C., Monastera, V. M., Derry, L. A., & Chadwick, O. A. (2007). Importance of atmospheric inputs and Fe-oxides in controlling soil uranium budgets and behavior along a Hawaiian chronosequence. *Chemical Geology*, 244(3-4), 691-707.
- Poore, R. Z., Pavich, M. J., & Grissino-Mayer, H. D. (2005). Record of the North American southwest monsoon from Gulf of Mexico sediment cores. *Geology*, 33(3), 209-212.
- Rasmussen, C., Southard, R. J., & Horwath, W. R. (2005). Modeling energy inputs to predict pedogenic environments using regional environmental databases. *Soil Science Society of America Journal*, 69(4), 1266-1274.
- 710 Rasmussen, C., & Tabor, N. J. (2007). Applying a quantitative pedogenic energy model across a range of environmental gradients. *Soil Science Society of America Journal*, 71(6), 1719-1729.
- Reagan, M. K., McClelland, W. C., Girard, G., Goff, K. R., Peate, D. W., Ohara, Y., & Stern, R. J. (2013). The geology of the southern Mariana fore-arc crust: Implications for the scale of Eocene volcanism in the western Pacific. *Earth and Planetary Science Letters*, 380, 41-51.
- 715 Renne, P. R., Deino, A. L., Hilgen, F. J., Kuiper, K. F., Mark, D. F., Mitchell, W. S., ... & Smit, J. (2013). Time scales of critical events around the Cretaceous-Paleogene boundary. *Science*, 339(6120), 684-687.
- Retallack, G. J. (1999). Postapocalyptic greenhouse paleoclimate revealed by earliest Triassic paleosols in the Sydney Basin, Australia. *Geological Society of America Bulletin*, 111(1), 52-70.
- Retallack, G. J. (2001). *Soils of the past. An introduction to palaeopedology*. Blackwell Science Limited, Oxford, England.
- 720 Retallack, G. J. (2009). Refining a pedogenic-carbonate CO₂ paleobarometer to quantify a middle Miocene greenhouse spike. *Palaeogeography, Palaeoclimatology, Palaeoecology*, 281(1-2), 57-65.
- Roehler, H. W. (1993). Eocene climates, depositional environments, and geography, greater Green River Basin, Wyoming, Utah, and Colorado. *United States Geological Survey, Professional Paper*, (1506-F).
- 725 Robinson, P., Gunnell, G. F., Walsh, S. L., Clyde, W. C., Storer, J. E., Stucky, R. K., ... & Woodburne, M. O. (2004). Wasatchian through Duchesnean biochronology. *Late Cretaceous and Cenozoic Mammals of North America*. Columbia University Press, New York, 106-155.
- Royer, D. L. (1999). Depth to pedogenic carbonate horizon as a paleoprecipitation indicator?. *Geology*, 27(12), 1123-1126.
- Royer, D. L., Wing, S. L., Beerling, D. J., Jolley, D. W., Koch, P. L., Hickey, L. J., & Berner, R. A. (2001). Paleobotanical evidence for near present-day levels of atmospheric CO₂ during part of the Tertiary. *Science*, 292(5525), 2310-2313.
- 730 Royer, D. L. (2003). Estimating latest Cretaceous and Tertiary atmospheric CO₂ from stomatal indices. In S.L. Wing, P.D. Gingerich, B. Schmitz, & E. Thomas (Eds.), *Causes and Consequences of Globally Warm Climates in the Early Paleogene*, (pp. 79-93). Geological Society of America Special Paper 369.
- 735 Sayyed, M. R. G., & Hundekari, S. M. (2006). Preliminary comparison of ancient bole beds and modern soils developed upon the Deccan volcanic basalts around Pune (India): Potential for palaeoenvironmental reconstruction. *Quaternary International*, 156, 189-199.
- Schiermeier, Q. (2020). Global methane levels soar to record high. *Nature*. doi: 10.1038/d41586-020-02116-8.



- Sheldon, N. D., Retallack, G. J., & Tanaka, S. (2002). Geochemical climofunctions from North American soils and application to paleosols across the Eocene-Oligocene boundary in Oregon. *The Journal of Geology*, 110(6), 687-696.
- 740 Sheldon, N. D. (2006). Abrupt chemical weathering increase across the Permian–Triassic boundary. *Palaeogeography, Palaeoclimatology, Palaeoecology*, 231(3-4), 315-321.
- Sheldon, N. D., & Tabor, N. J. (2009). Quantitative paleoenvironmental and paleoclimatic reconstruction using paleosols. *Earth-Science Reviews*, 95(1-2), 1-52.
- 745 Sheldon, N. D., Smith, S. Y., Stein, R., & Ng, M. (2020). Carbon isotope ecology of gymnosperms and implications for paleoclimatic and paleoecological studies. *Global and Planetary Change*, 103060.
- Smith, M. E., Carroll, A. R., & Singer, B. S. (2008). Synoptic reconstruction of a major ancient lake system: Eocene Green River Formation, western United States. *GSA bulletin*, 120(1-2), 54-84.
- Smith, M. E., Chamberlain, K. R., Singer, B. S., & Carroll, A. R. (2010). Eocene clocks agree: Coeval $^{40}\text{Ar}/^{39}\text{Ar}$, U-Pb, and astronomical ages from the Green River Formation. *Geology*, 38(6), 527-530.
- 750 Smith, M. E., Carroll, A. R., Jicha, B. R., Cassel, E. J., & Scott, J. J. (2014). Paleogeographic record of Eocene Farallon slab rollback beneath western North America. *Geology*, 42(12), 1039-1042.
- Smith, M. E., Carroll, A. R., & Scott, J. J. (2015). Stratigraphic expression of climate, tectonism, and geomorphic forcing in an underfilled lake basin: Wilkins Peak Member of the Green River Formation. In *Stratigraphy and Paleolimnology of the Green River Formation, Western USA* (pp. 61-102). Springer, Dordrecht.
- 755 Smith, R. Y., Greenwood, D. R., & Basinger, J. F. (2010). Estimating paleoatmospheric pCO_2 during the Early Eocene Climatic Optimum from stomatal frequency of *Ginkgo*, Okanagan Highlands, British Columbia, Canada. *Palaeogeography, Palaeoclimatology, Palaeoecology*, 293, 120-131.
- Smith, R. Y., Basinger, J. F., and Greenwood, D. R. (2012). Early Eocene plant diversity and dynamics in the Falkland flora, Okanagan Highlands, British Columbia, Canada, *Palaeobiodiversity and Palaeoenvironments*, 92(3), 309–328, <https://doi.org/10.1007/s12549-011-0061-5>.
- 760 Snoke, A. W., Steidtmann, J. R., & Roberts, S. M. (1993). Geologic history of Wyoming within the tectonic framework of the North American Cordillera. *Geology of Wyoming: Geological Survey of Wyoming Memoir*, 5, 2-56.
- Spicer, R. A., Valdes, P. J., Spicer, T. E. V., Craggs, H. J., Srivastava, G., Mehrotra, R. C., & Yang, J. (2009). New developments in CLAMP: calibration using global gridded meteorological data. *Palaeogeography, Palaeoclimatology, Palaeoecology*, 283(1-2), 91-98.
- 765 Stein, R. A., Sheldon, N. D., & Smith, S. (2019). Rapid response to anthropogenic climate change by *Thuja occidentalis*: implications for past climate reconstructions and future climate predictions. *PeerJ*, 7, e7378.
- Stein, R. A., Sheldon, N. D., & Smith S. (2021). C_3 plant carbon isotope discrimination does not respond to CO_2 concentration on decadal to centennial timescales. *New Phytologist*, 229 (5), 2576-2585 doi: 10.1111/nph.17030
- Steinhorsdottir, M., Vajda, V., Pole, M., & Holdgate, G. (2019). Moderate levels of Eocene pCO_2 indicated by Southern Hemisphere fossil plant stomata. *Geology*, 47(10), 914-918.



- 770 Surdam, R. C., & Stanley, K. O. (1979). Lacustrine sedimentation during the culminating phase of Eocene lake Gosiute, Wyoming (Green River Formation). *Geological Society of America Bulletin*, 90(1), 93-110.
- Tipple, B. J., Meyers, S. R., & Pagani, M. (2010). Carbon isotope ratio of Cenozoic CO₂: A comparative evaluation of available geochemical proxies. *Paleoceanography*, 25(3).
- Tu, T. N., Derenne, S., Largeau, C., Bardoux, G., & Mariotti, A. (2004). Diagenesis effects on specific carbon isotope composition of plant n-alkanes. *Organic Geochemistry*, 35(3), 317-329.
- 775 Van Houten, F. B. (1944). Stratigraphy of the Willwood and Tatman formations in northwestern Wyoming. *Bulletin of the Geological Society of America*, 55(2), 165-210.
- Vinogradov, A. P. (1959). Geochemistry of rare and dispersed chemical elements in soils. Consultants Bureau, New York.
- West, C. K., Greenwood, D. R., Reichgelt, T., Lowe, A. J., Vachon, J. M., Basinger, J. F. (2020). Paleobotanical proxies for early Eocene climates and ecosystems in northern North America from middle to high latitudes, *Climate of the Past*, 16, 1387-1410.
- 780 Wilf, P. (1997). When are leaves good thermometers? A new case for leaf margin analysis. *Paleobiology*, 373-390.
- Wilf, P., Wing, S. L., Greenwood, D. R., & Greenwood, C. L. (1998). Using fossil leaves as paleoprecipitation indicators: an Eocene example. *Geology*, 26(3), 203-206.
- Wilf, P. (2000). Late Paleocene–early Eocene climate changes in southwestern Wyoming: Paleobotanical analysis. *Geological Society of America Bulletin*, 112(2), 292-307.
- 785 Wing, S. L., & Greenwood, D. R. (1993). Fossils and fossil climate: the case for equable continental interiors in the Eocene. *Philosophical Transactions of the Royal Society of London. Series B: Biological Sciences*, 341(1297), 243-252.
- Wing, S. L., Harrington, G. J., Smith, F. A., Bloch, J. I., Boyer, D. M., & Freeman, K. H. (2005). Transient floral change and rapid global warming at the Paleocene-Eocene boundary. *Science*, 310(5750), 993-996.
- 790 Wing, S. L., & Currano, E. D. (2013). Plant response to a global greenhouse event 56 million years ago. *American Journal of Botany*, 100(7), 1234-1254.
- Witkowski, C. R., Weijers, J. W., Blais, B., Schouten, S., & Damsté, J. S. S. (2018). Molecular fossils from phytoplankton reveal secular PCO₂ trend over the Phanerozoic. *Science advances*, 4(11), eaat4556.
- 795 Wolfe, J. A. (1979). Temperature parameters of humid to mesic forests of eastern Asia and relation to forests of other regions of the northern hemisphere and Australasia. *United States Geological Survey Professional Paper*, 1106, 1-37.
- Wolfe, J. A. (1993). A method of obtaining climatic parameters from leaf assemblages. *United States Geological Survey Bulletin*, 2040, 1-73.
- 800 Wolfe, J. A., Forest, C. E., & Molnar, P. (1998). Paleobotanical evidence of Eocene and Oligocene paleoaltitudes in midlatitude western North America. *Geological Society of America Bulletin*, 110(5), 664-678.



- Wood II H. E., Chaney, R. W., Clark, J., Colbert, E. H., Jepsen, G. L., Reeside Jr, J. B., ... & Committee. (1941). Nomenclature and correlation of the North American continental Tertiary. *Bulletin of the Geological Society of America*, 52(1), 1-48.
- 805 Zachos, J. C., Dickens, G. R., & Zeebe, R. E. (2008). An early Cenozoic perspective on greenhouse warming and carbon-cycle dynamics. *Nature*, 451(7176), 279-283.
- Zhang, L., Wang, C., Wignall, P. B., Kluge, T., Wan, X., Wang, Q., & Gao, Y. (2018). Deccan volcanism caused coupled $p\text{CO}_2$ and terrestrial temperature rises, and pre-impact extinctions in northern China. *Geology*, 46(3), 271-274.
- Zhu, J., Poulsen, C. J., & Tierney, J. E. (2019). Simulation of Eocene extreme warmth and high climate sensitivity through cloud feedbacks. *Science advances*, 5(9), eaax1874.
- 810

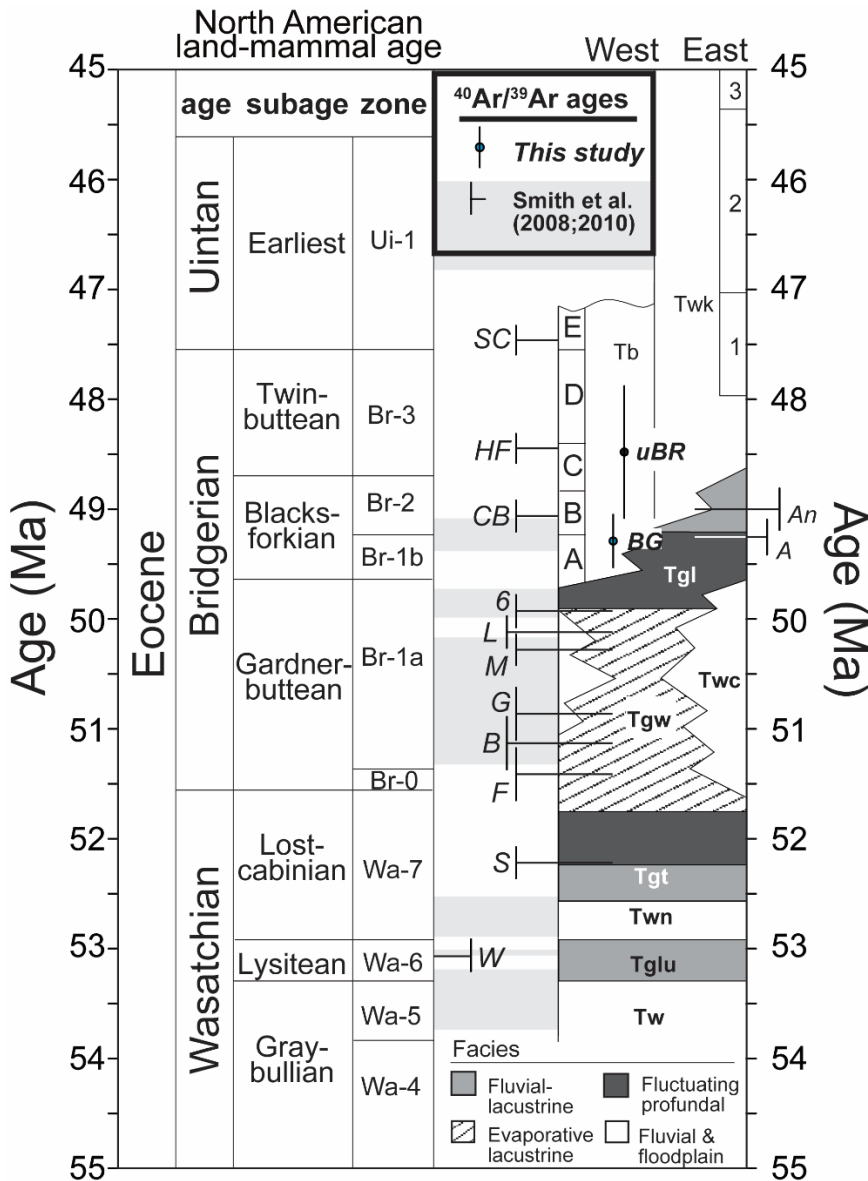


Figure 1: Age model of the Eocene Wyoming. North American Land Mammal Age (NALMA) is shown for context. Upper Blue Rim is shown as “uBR” and the blue-green marker is depicted as “BG,” and both are shown with dots and error bars. Dates from Smith et al. (2008; 2010) are shown in perpendicular lines. The abbreviations included are designated as follows. Green River Formation: *Tglu* Luman Member, *Tgt* Tipton Member, *Tgl* Laney Member. Wasatch Formation: *Tw* “Main body,” *Twn* Niland Tongue, *Twc* Cathedral Bluffs Member, *Tb* Bridger Formation, *Twk* Washakie Formation. Tuff beds as measured in Smith et al. (2008; 2010) are denoted as: *W* Willwood, *S* Scheggs, *R* Rife, *F*, Firehole, *B* Boar, *G* Grey, *M* Main, *L* Layered, *6* Sixth, *A* Analcite, *CB* Church Butte, *HF* Henrys Fork, and *SC* Sage Creek.

815

820

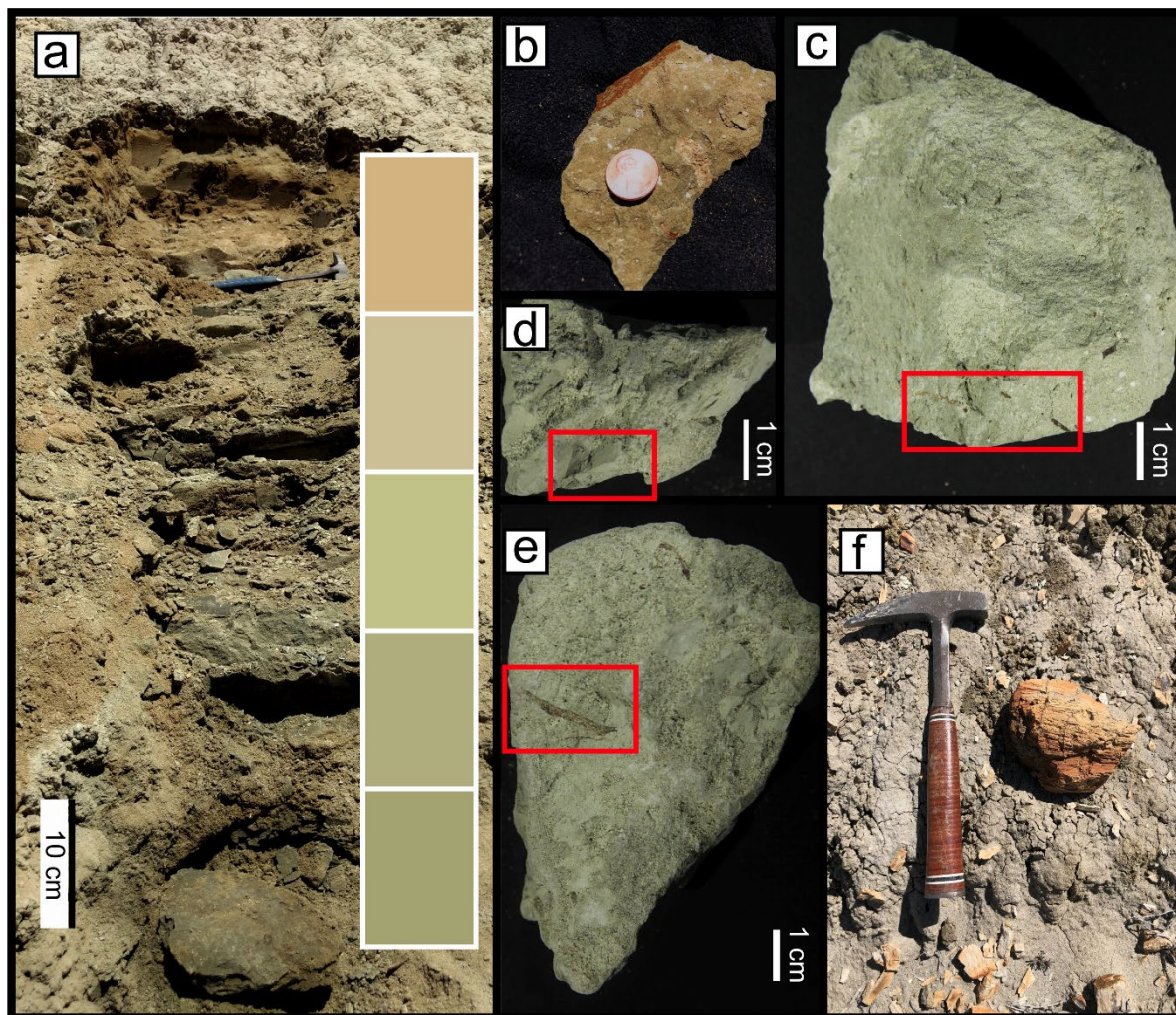
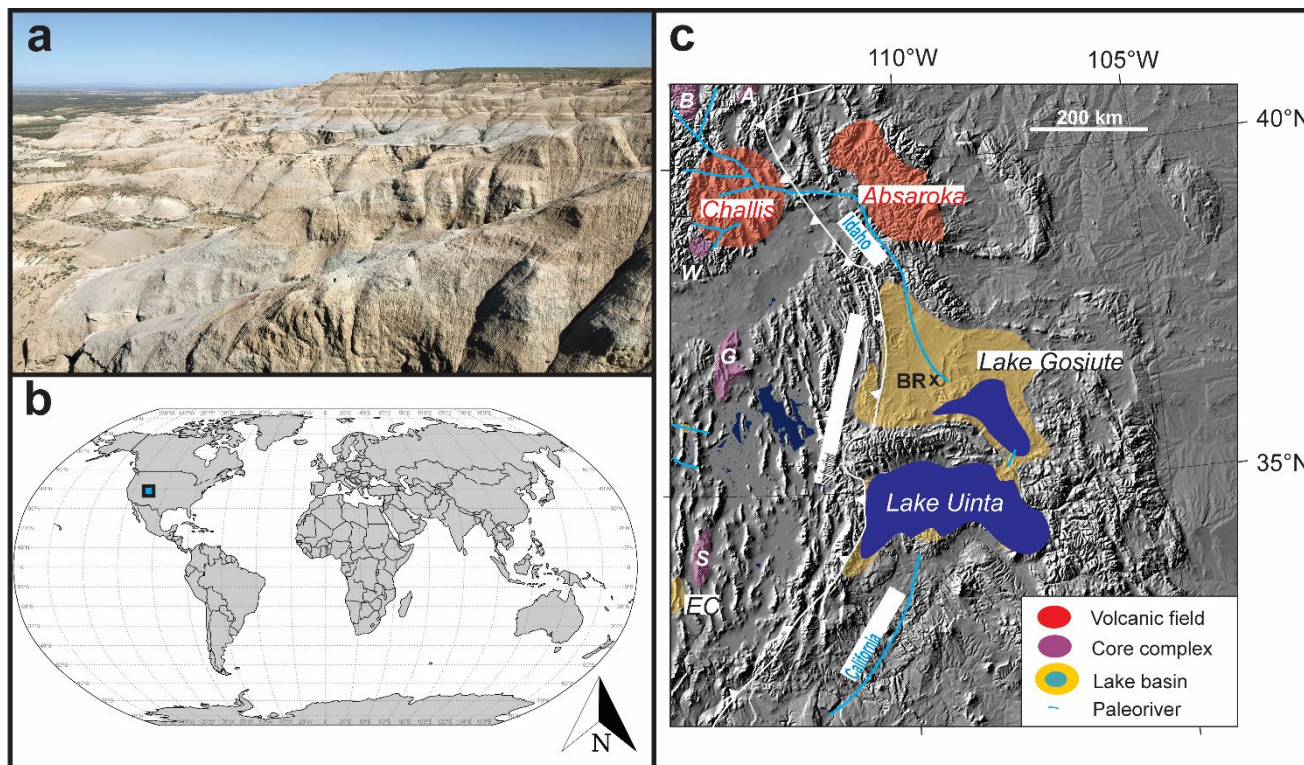


Figure 2: Paleosol images and features. (a) Full profile of 19BRWY3 with rock hammer for scale, (b) shows drab-haloed root trace from 19BRWY-2UB, (c) A-horizon fine organic rootlets in red box from 19BRWY2UA, (d) slickensides on 19BRWY1UA, (e) rhizoliths from 19BRWY1UA, and (f) mineralized wood with rock hammer for scale, excavated ~3 m above 19BRWY1.

825

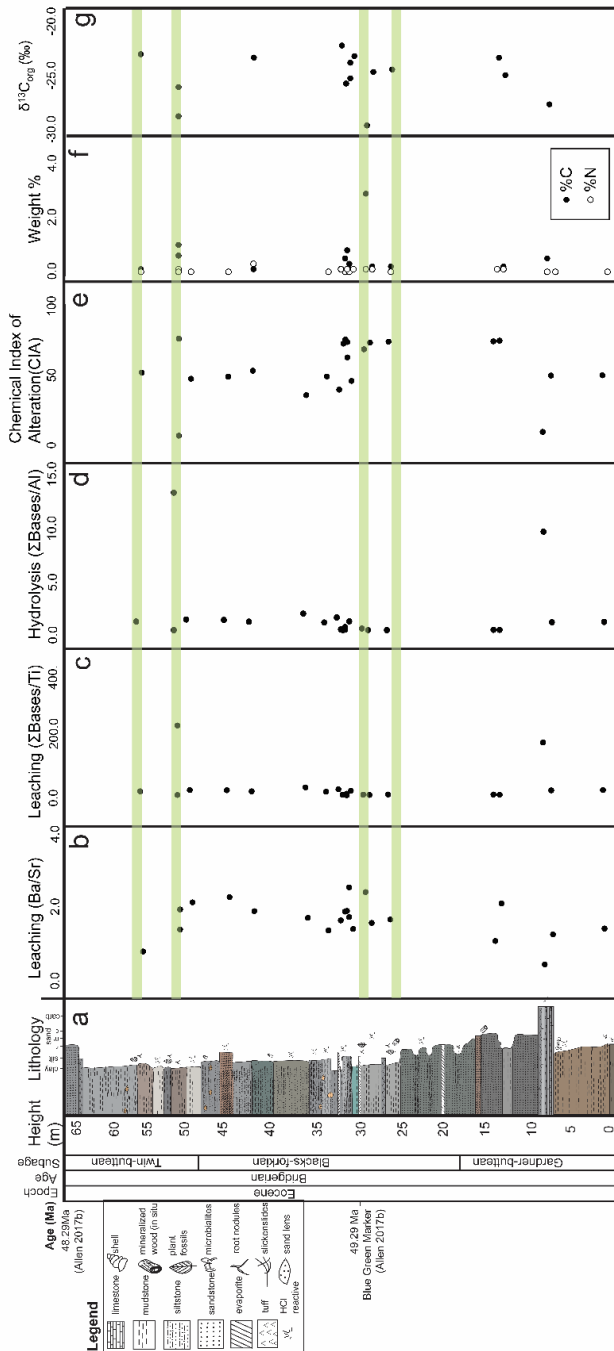


830

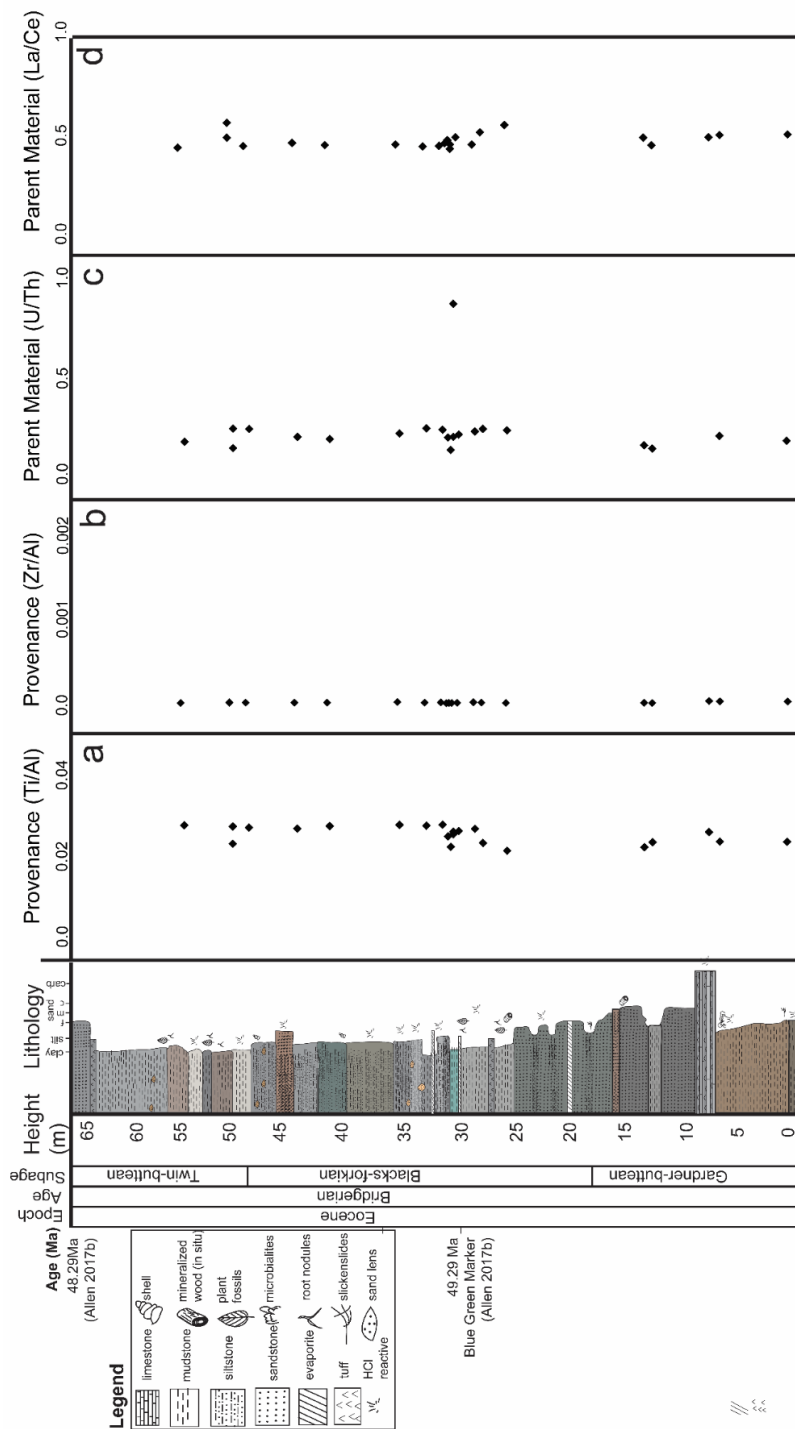
835

Figure 3: Map and profile of Blue Rim escarpment. (a) Landscape image of the escarpment from the uppermost strata. (b) Location of Blue Rim escarpment (blue square) at present, in context of the present tectonic configuration of the world using a Robinson projection map. (c) Shaded relief map of the North American Cordillera showing the paleogeographic position of the Blue Rim (BR) relative to major paleorivers, lake basins, and tectonic elements. EC refers to early Bridgerian Elderberry Canyon local fauna of Emry (1990). Core complexes occur near the Cordilleran paleodivide: *B* – Bitterroot; *A* – Anaconda; *W* – Wildhorse; *G* – Albion-Raft River-Grouse Creek; *S* – Snake. Note that the Bridger Formation at Blue Rim represents the topsets of the Sand Butte delta (cf. Smith et al., 2008). Paleorivers summarized from Henry et al. (2012), Dickinson et al. (2012) and Chetel et al. (2011).

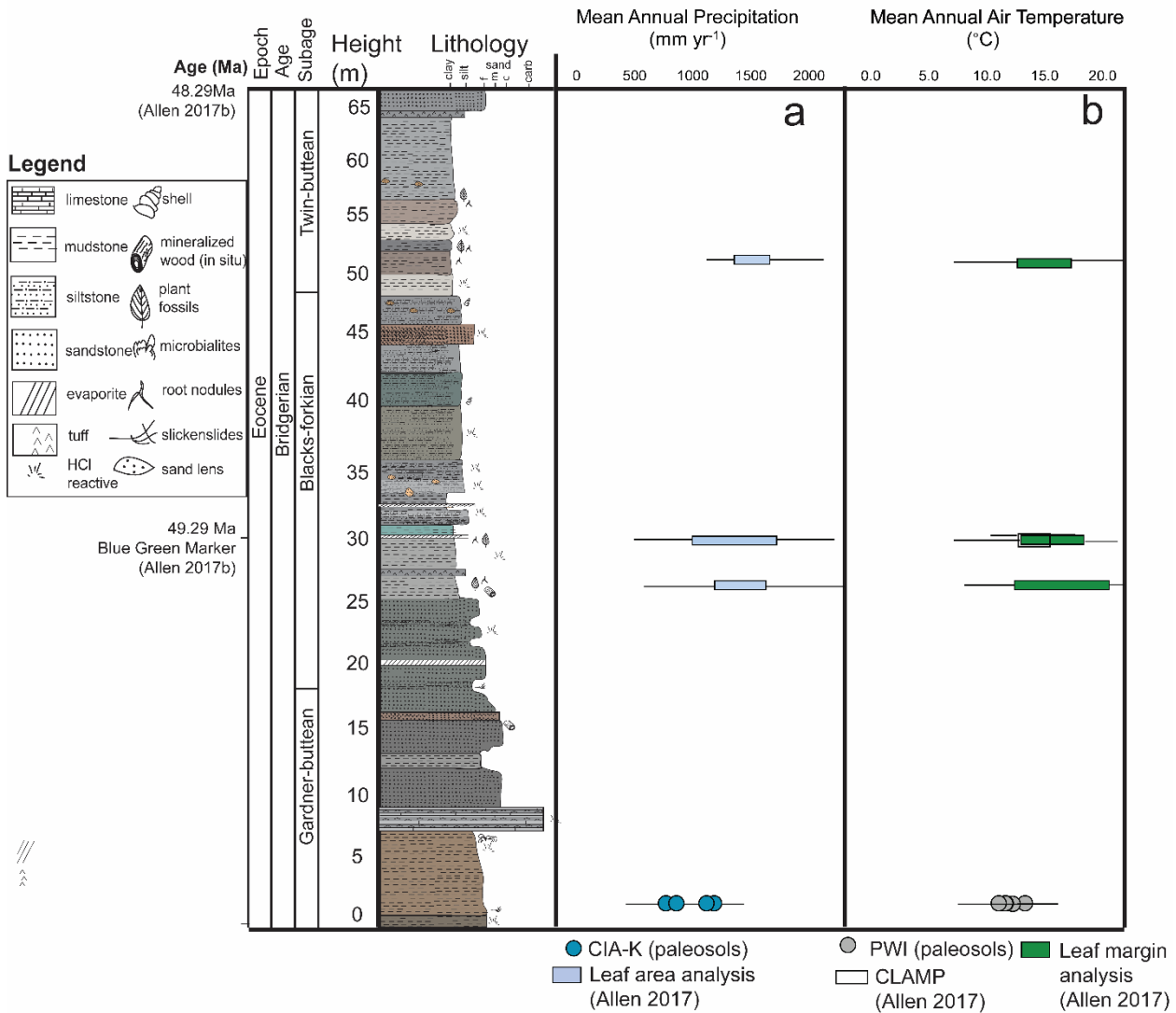
840



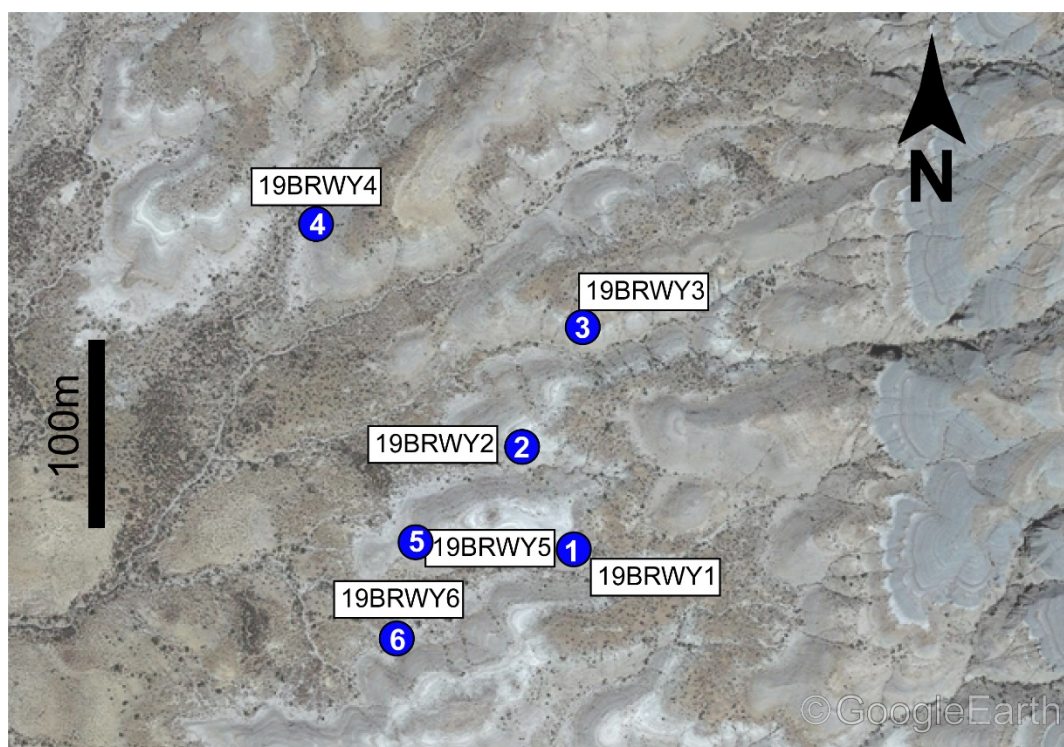
845 **Figure 4: Stratigraphy with sedimentary geochemistry.** (a) Stratigraphic column at the Blue Rim escarpment of the Bridger Formation. Geochemistry including (b) leaching, calculated using molar ratios of Ba/Sr, (c) leaching, calculated using the ratio of the sum of bases to Titanium, (d) hydrolysis, calculated using the ratio of the sum of bases to Aluminum, (e) chemical index of alteration to measure weathering (Equation 1), (f) weight % Carbon (black circles) and % Nitrogen (white circles), (g) $\delta^{13}\text{C}_{\text{org}}$ values. Light green transparent areas show stratigraphic levels containing plant fossils.



850 **Figure 5: Stratigraphy with parent material and provenance proxies.** (a) Provenance using molar ratios of Ti/Al, (b) provenance using molar ratios of Zr/Al, (c) parent material using molar ratios of U/Th, (d) parent material using molar ratios of La/Ce.



855 **Figure 6 Stratigraphic column with climate proxies.** (a) Reconstructed mean annual precipitation (mm yr⁻¹), and (b) mean annual air temperature (°C). The boxes are ranges reconstructed for physiognomic proxies, and the circles are values reconstructed using paleosols. The lines for both are established errors for the proxies used.



865

Figure 7: Lateral extent of paleosols. Included are paleosols 19BRWY1-6, atop image of Blue Rim escarpment topography, with a 100 m scalebar. Paleosol numbers are noted in white text on blue circles. Image taken in Google earth V 9.123.0.2 (July 2019). Wyoming, USA. 41°48'02"N, 109°35'36"W, eye altitude 2625 m. © Google Earth.

870

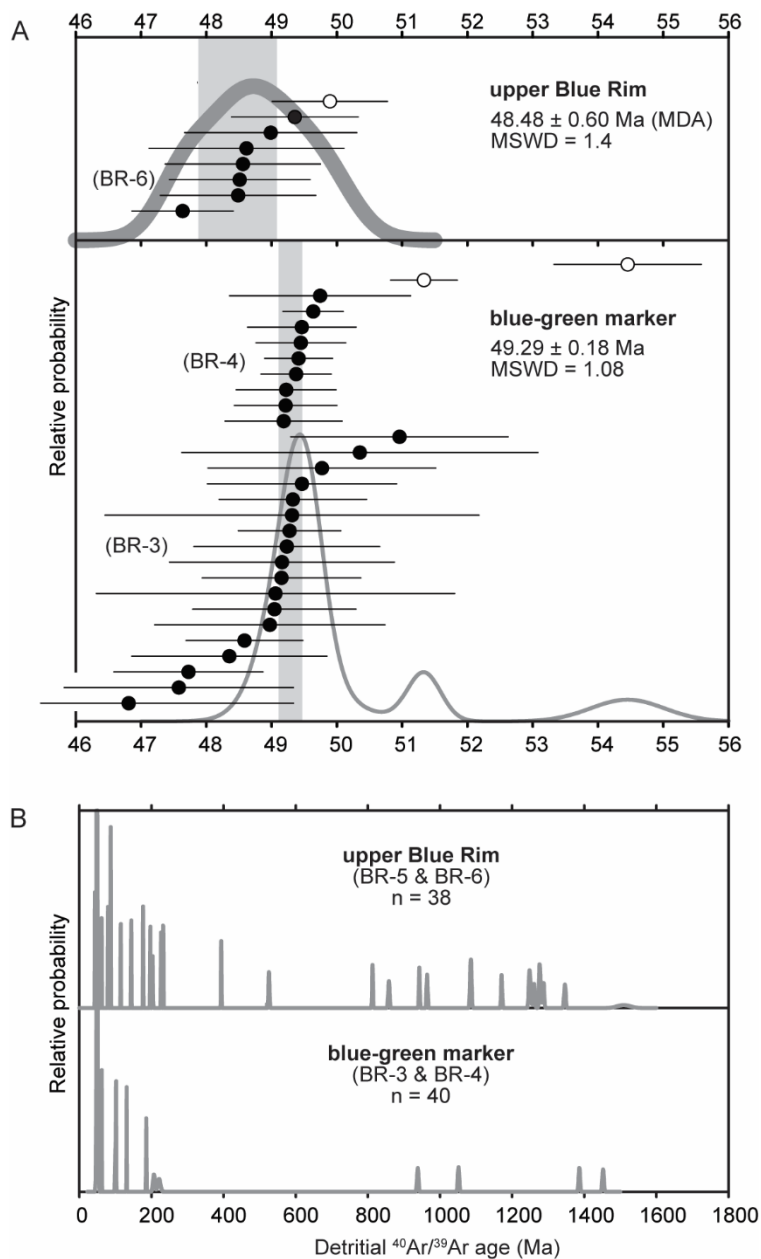


Figure 8: $^{40}\text{Ar}/^{39}\text{Ar}$ geochronology: a) Relative probability plots of Eocene-aged sanidine from the volcanoclastic-lacustrine blue-green marker and an overlying pumice-bearing volcanoclastic sandstone (sample BR-6); b) Relative probability plot of $^{40}\text{Ar}/^{39}\text{Ar}$ ages for detrital feldspar grains from the middle and upper Blue Rim, showing Phanerozoic and late Paleozoic ages characteristic of the Idaho paleoriver (cf. Chetel et al., 2011).

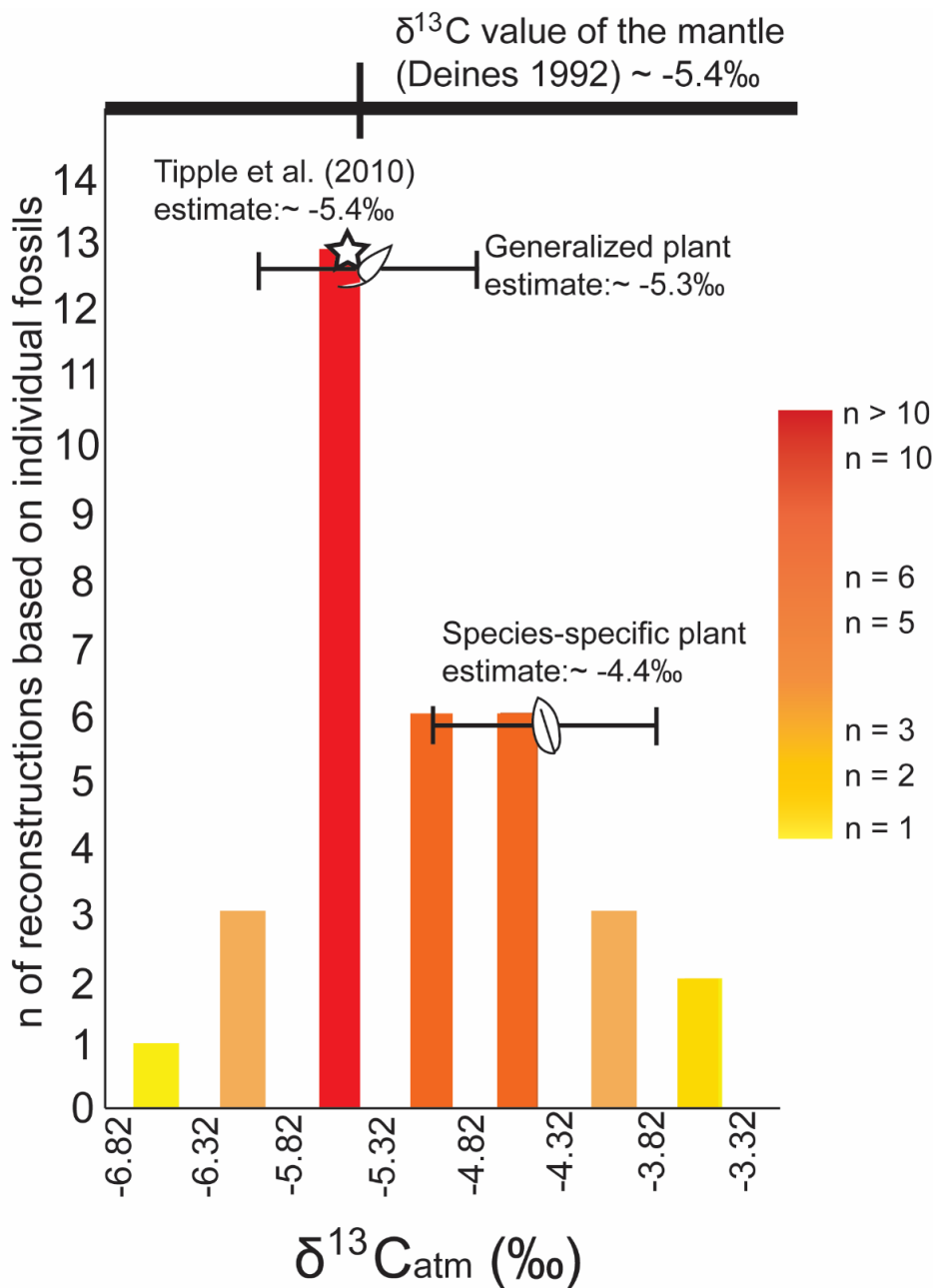


Figure 9: $\delta^{13}C_{atm}$ as reconstructed from $\delta^{13}C_{leaf}$ of the Blue Rim fossil flora. Reconstructions utilized the generalized relationship between $\delta^{13}C_{atm}$ and $\delta^{13}C_{plant}$ (Arens et al. 2000; $n = 34$; Equation 8). The species-specific mean and standard deviation are shown (based on *Lygodium* and *Populus* fossils, $n = 8$), as are the generalized plant mean and standard deviation. The Tipple et al. (2010) foraminiferal reconstruction is denoted in a star, and the $\delta^{13}C$ value of the mantle is shown above (Deines 1992).

880

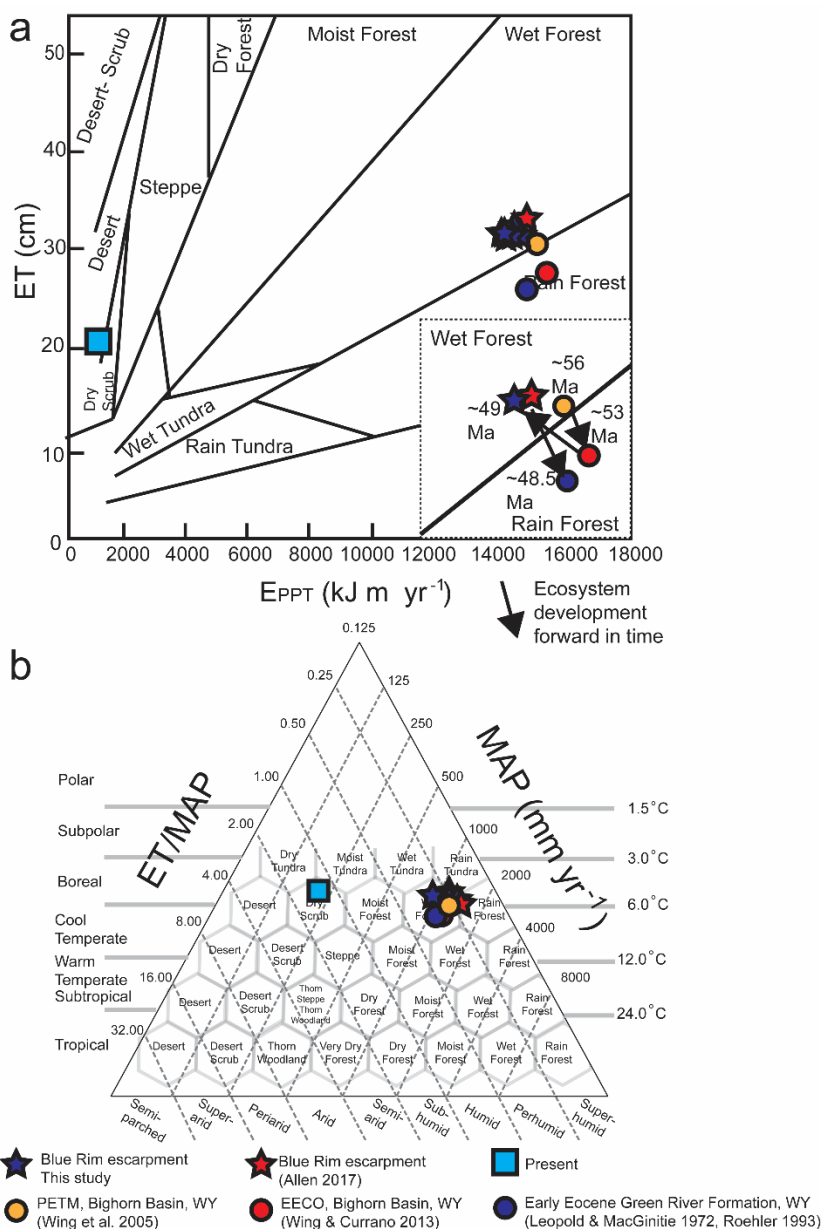


Figure 10: Ecosystem level characterization of Blue Rim escarpment and other Cenozoic Wyoming ecosystems.

885 Paleosol-based (a) Floral Humidity Province and (b) Holdridge life zones (Holdridge 1967) in blue stars. (a) includes inset
 showing climate progression over time, with (1) showing the PETM (Bighorn Basin, ~56 Ma), (2) the EECO (Bighorn
 Basin, ~53 Ma), (3) this site (~49 Ma) and (4) the latest stage of Lake Gosiute (Green River Formation, ~48.5 Ma; Smith et
 al., 2008). Comparative studies for this region based on nearby temperature and precipitation reconstructions are shown in
 yellow, red and blue circles, while the climate of the present (as measured in Rock Springs, Wyoming, U.S.A.) is shown in
 890 light blue squares. Average values from Allen (2017b) using leaf margin analysis to reconstruct MAAT and leaf area
 analysis to reconstruct MAP is shown in red stars.



895

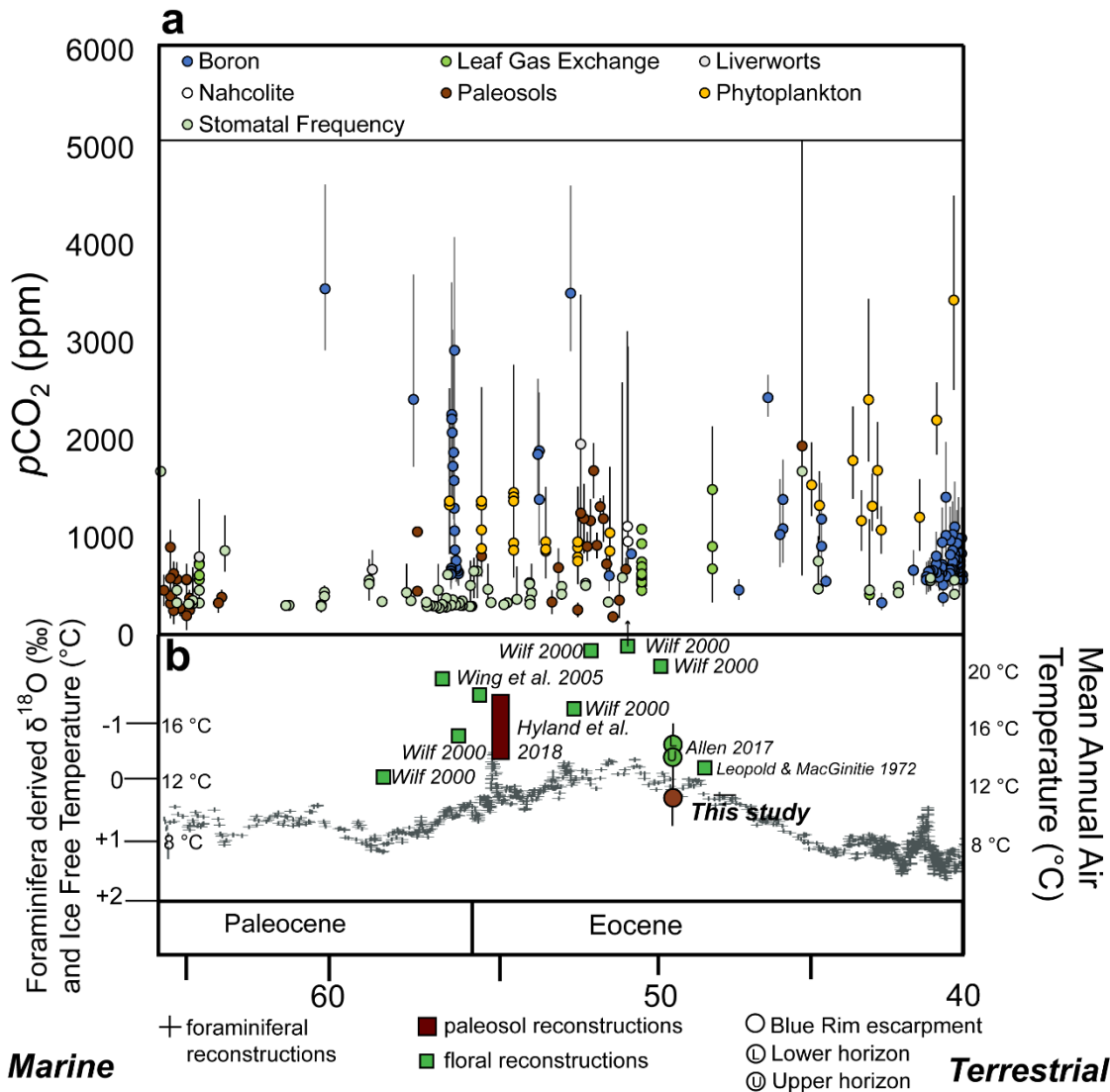


Figure 11: Paleoclimate reconstructions from Blue Rim escarpment in the context of the evolution of climate from 66 to 40 Ma. (a) $p\text{CO}_2$ from 66 to 40 Ma based on multiple proxies compiled on paleo- CO_2 .org (McElwain 1998; Ekart et al., 1999; Pearson & Palmer 2000; Royer et al., 2001; Greenwood et al., 2003; Royer 2003; Pagani et al., 2005; Lowenstein & Demicco 2006; Fletcher et al., 2008; Zachos et al., 2008; Franks & Beerling 2009; Retallack 2009; Bijl et al., 2010; Smith et al., 2010; Grein et al., 2011; Pagani et al., 2011; Hyland & Sheldon 2013; Hyland et al., 2013; Huang et al., 2013; Franks et al., 2014; Maxbauer et al., 2014; Jagniecki et al., 2015; Anagnostou et al., 2016; Barclay & Wing 2016; Liu et al., 2016; Kowalczyk et al., 2018; Witkowski et al., 2018; Zhang et al., 2018; Milligan et al., 2019; Steinthorsdottir et al., 2019; Haynes et al., 2020; Henehan et al., 2019; Henehan et al., 2020). (b) marine $\delta^{18}\text{O}$ and ice-free temperature reconstructions based on foraminiferal data (Zachos et al., 2008) and mean annual air temperatures reconstructed from physiognomic (green) and paleosol (brown) proxies in the Paleocene and Eocene.



910

Table 1. Summary of single crystal sanidine $^{40}\text{Ar}/^{39}\text{Ar}$ analyses: Bridger Formation, Blue Rim, WY.

| (sample) | material | Latitude | Longitude | n | MSWD | Weighted mean age (Ma) | $\pm 2\sigma$ [†] | $\pm 2\sigma$ [‡] |
|-----------------------------|---------------------|------------|-------------|----------|----------|------------------------|----------------------------|----------------------------|
| upper Blue Rim | | | | | | | | |
| (BR-6) | sandstone | 41.8213° N | 109.5949° W | 6 of 18 | 0.93 | 48.29 | ± 0.45 | ± 0.48 |
| (BR-5) | sandstone | 41.8210° N | 109.5952° W | 0 of 19 | detrital | n.a. | | |
| blue-green marker | | | | | | | | |
| (BR-4) | pumiceous sandstone | 41.8218° N | 109.5972° W | 9 of 20 | 0.24 | 49.43 | ± 0.23 | ± 0.28 |
| (BR-3) | basal sandstone | 41.7987° N | 109.5834° W | 18 of 20 | 1.20 | 48.98 | ± 0.38 | ± 0.41 |
| Blue-green marker composite | | | | 27 of 40 | 1.08 | 49.29 | ± 0.18 | ± 0.24 |

Notes: All ages calculated relative to the 28.201 Ma age for FCs using the equations of Kuiper et al. (2008) and Renne et al. (1998), using the decay constants of Min et al. (2000), and are shown with 2σ analytical and fully propagated uncertainties, which incorporate decay constant and intercalibration uncertainties. Neutron flux monitor: FCs-Fish Canyon Tuff sanidine, Cf. Table 2 for analytical details. Ages in bold reflect interpreted depositional ages.

[†]Analytical uncertainty.

[‡]Fully propagated uncertainty.